University of Neuchâtel
Physics Department

Superconducting Tunnel Junctions as Detectors for Mass Spectrometry

Thesis by

Yvan Gonin

in partial Fulfillment of the Requirements for the Degree of

Docteur ès Sciences

Neuchâtel, December 2002

Thesis advisor : Prof. Dr. J.-L. Vuilleumier
Institut de Physique, Université de Neuchâtel, Neuchâtel

Co-advisors : PD Dr. Damian Twerenbold
Institut de Physique, Université de Neuchâtel, Neuchâtel

Dr. Eugenie Kirk
Paul Scherrer Institut, Villigen

Superconducting Tunnel Junctions as Detectors for Mass Spectrometry

IMPRIMATUR POUR LA THESE

Superconducting Tunnel Junctions as Detectors for Mass Spectrometry

de M. Yvan Gonin

UNIVERSITE DE NEUCHATEL

FACULTE DES SCIENCES

La Faculté des sciences de l'Université de Neuchâtel sur le rapport des membres du jury,

Mme E. Kirk (PSI),
MM. J.-L. Vuilleumier (directeur de thèse)
et D. Twerenbold

autorise l'impression de la présente thèse.

Neuchâtel, le 4 mars 2003

Le doyen:

F. Zwahlen

To my dear wife Cynthia and Chloé

Contents

Units, constants and abbreviations

Units

Dalton (Da) : commonly used unit in mass spectrometry, equivalent to $1/16^{th}$ of the mass of a ^{16}O atom, that is about the mass of a proton.

Constants

h : $h = 6.6262 \cdot 10^{-34}$ J·s Planck's constant

Abbreviations

GMU	:	George Mason University, Fairfax, VI, USA
PSI	:	Paul Scherrer Institut, Villigen, Switzerland
NIST	:	National Institute of Standards and Technology, Boulder, CO, USA
LLNL	:	Lawrence Livermore National Laboratory, Livermore, CA, USA
IPH	:	Institut de Physique, Université de Neuchâtel, Switzerland
MS	:	Mass Spectrometry
ToF	:	Time-of-Flight
MALDI	:	Matrix-Assisted Laser Desorption / Ionization
SEM	:	Secondary Electron Multiplier
MCP	:	MicroChannel Plate
STJ	:	Superconducting Tunnel Junction
SIS	:	Superconductor – Insulator – Superconductor
NIS	:	Normal conductor – Insulator – Superconductor
TES	:	Transition Edge Sensor
PCB	:	Printed Circuit Board
ADR	:	Adiabatic Demagnetization Refrigerator
MBE	:	Molecular Beam Epitaxy

Introduction

Biochemistry and molecular biology are sciences which are experiencing a rapid growth in terms of discoveries and markets. At the same time, instruments and techniques intended for this research are undergoing a fast development. Among those instruments, mass spectrometers play an important role and the last generation profiles itself with a huge potential for the future.

Mass spectrometry is a very powerful tool to determine the masses of molecules by analyzing their movement in an electrical or/and magnetic field. Several kinds of spectrometers exist : for instance Time-of-Flight (ToF), Fourier Transform (FT) or Quadrupole mass analyzer. They all are composed of :

1. an ion source,

2. a mass analyzer,

3. an ion detector.

The role of the ion source is to vaporize and ionize the molecules. In the seventies, electron impact (EI) and chemical ionization (CI) were used. Unfortunately the molecular weight was limited to about 800 Da. Later on, different techniques were developed, either liquid-phase ion sources (Electrospray Ionization (ESI), Thermospray (TS), etc), or solid-state ion sources (Field Desorption (FD), Fast Atom Bombardment (FAB), etc), pushing the limit up to 50 kDa. In 1987, a major advance was made by Karas, Hillenkamp *et al.* [1] : they successfully desorbed molecules weighing more than 500 kDa by diluting them into a matrix absorbing laser light which ionizes them. This technique was called MALDI (Matrix-Assisted Laser Desorption / Ionization). Both solid or liquid MALDI are used.

The ions are then analyzed in the mass analyzer according to different principles. One can mention quadrupole mass analyzers, Fourier Transform or magnetic sector mass analyzers. Time-of-Flight are also widely used. In this case, the ions being desorbed are accelerated with an electrical field and « fly » through the spectrometer until they hit a detector. The time-of-flight is easily converted to mass. More information is found in chapter I.

The final step consists of detecting the ions. Classical detectors are usually based on the secondary electron emission followed by a cascade of electrons providing a gain of 10^4 to 10^8. The basic operation principles are identical for many ions detectors, except for a few details. This is explained in chapter 1. The major problem of these devices is their loss of sensitivity for massive macromolecules which decreases with the speed of the incoming particle. For a given acceleration voltage, heavy molecules travel slower, inducing a lower signal. Molecules heavier than 50 kDa are not detected anymore, so that the study of biomolecules like DNA or oligonucleotides cannot be performed.

To solve this problem, Twerenbold proposed, in 1995, the use of cryogenic detectors, previously developed for particle physics and astrophysical applications [2]. The detection mechanism is radically different, based on the variation of the internal energy upon impact leading to a 100% detection efficiency; this hypothesis has been verified [3, 4, 5]. One year later, the first experiment, proving the above-mentioned proposition, was performed by a Neuchâtel / GMU / PSI collaboration. For the first time ever, Lyzozyme proteins were detected with a cryogenic detector, in that case with tin superconducting tunnel junctions [6].

Shortly after, a second experiment was performed by a NIST / Neuchâtel / GMU collaboration where another type of cryogenic detector was tested with Lyzozyme, BSA (Bovine Serum Albumin) and IgG (Immunoglobulin G) : a hot-electron microcalorimeter. The same results were obtained and charge state separation was clearly seen. Results were published in Nature [7] and presented at the LTD-7 Conference in Munich [8].

Continuing that way, new photolithographic techniques were used to improve tin STJ, a new ion optics and a delayed extraction were installed to improve the performance of the mass spectrometer, especially by permitting discrimination between singly and doubly charged ions. Results have been presented at LTD-7 in Munich [9][1].

It is now well established in mass spectrometry that the best results for heavy molecules can be obtained with a MALDI ion source and a cryogenic detector. Other groups also came to that conclusion [10]. The mass analyzer can be a linear one but one can improve the resolution by using a reflectron.

We built two new linear mass spectrometers, one for solid MALDI using a UV laser, and a second one for liquid MALDI with an IR laser. We fabricated and tested several kinds of STJ on different substrates and cooled them down in a dilution refrigerator and in two cryostats, a $^3He/^4He$ and an ADR.

[1] All details of the history can be found in [11].

We developed arrays of 16 aluminum superconducting tunnel junctions with different photolithographic techniques (lift-off and wet-etching) on three different substrates : glass, polyimide and GaAs/AlAs stack. Several kinds of macromolecules were measured with our different arrays, using either solid or liquid MALDI.

Chapter 1 presents generalities on mass spectrometry and on MALDI technique (solid and liquid). At the end of this section, a few spectra of macromolecules are shown : they were captured using our previous array of Al junctions on a glass substrate (5 times 100 µm, diamond-shaped, in-line STJ). A quick overview of superconductivity and a little review on cryogenic detectors, including STJ, are given in chapters 2 and 3, respectively. Fabrication of the arrays of STJ, cryogenics and the experimental setup are described in chapter 4. Results are presented in chapter 5 and are divided in two parts : firstly results with polyimide substrates are described by comparing them with those on glass substrates ; secondly, a qualitative study of the energy deposited by X-rays and macromolecules in Al and Ta STJ is presented.

An article presenting the importance of mass spectrometry for macromolecules can be found in [12].

Chapter 1

Mass Spectrometry

A mass spectrometer is an apparatus used to determine the mass-to-charge ratio of molecules by analyzing their movement in an electrical and/or magnetic field. According to Newton's law, we have :

$$\vec{F} = m\ddot{\vec{x}} = q \cdot (\vec{E} + \dot{\vec{x}} \wedge \vec{B}) \tag{1.1}$$

where $\vec{E}$ and $\vec{B}$ are the electrical and magnetic fields respectively. Thus a charged ion can be accelerated by the former and deflected by the latter. The ratio m/q becomes important because those movements are mass and charge dependent.

As said in the introduction, many types of spectrometry exist, but we are going to restrict this chapter to the technique we work with, namely time-of-flight. A mass spectrometer can be described in three parts : the ion source, described in section 1.2., the mass analyzer, in section 1.1. and the detector in section 1.3.

1.1. Time-of-Flight mass spectrometer[2]

A ToF mass spectrometer is an instrument that measures the time needed by molecules, after acceleration in an electrical field, to reach the detector. According to the energy conservation law, $E = q \cdot U = mv^2/2$ where U is the acceleration voltage, q the charge of the ion[3], m its mass and v its velocity.

[2] A detailed review on Time-of-Flight mass spectrometry is given in [13].
[3] More precisely, a molecule is neutral. If it is charged, one speaks of an ion.

If the ions have to travel a distance d, the time-of-flight is :

$$t_{tof} = d \cdot \sqrt{\frac{m}{q} \cdot \frac{1}{2U}} \tag{1.2}$$

Therefore their time-of-flight is proportional to $\sqrt{m/q}$ and $1/\sqrt{U}$ and their energy to q and U. A sketch of a ToF mass spectrometer is shown in figure 1.1.

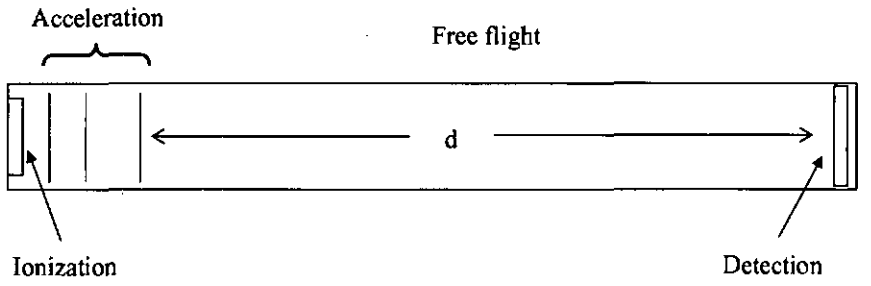

Fig. 1.1 : scheme of a ToF mass spectrometer showing the three steps of operation.

1.2. MALDI technique

Before 1987, techniques did not permit the desorption of molecules heavier than a few hundred kDa, because of fragmentation. That year, a major step forward was made when Karas and Hillenkamp's group announced a new desorption method : MALDI, for Matrix Assisted Laser Desorption / Ionization [1]. The molecules are dissolved in a matrix, either solid or liquid and placed in the spectrometer at high voltage. A short laser pulse gives the energy to desorb the molecules which can then be accelerated into the tube. Both solid and liquid phases of MALDI are treated in the next two sections.

The molecules to be analyzed are dissolved and mixed to a matrix, then dried and placed on a conducting sample holder and introduced into the spectrometer. A high voltage is applied to the sample holder and a short laser pulse desorbs the analyte.

Usually, a UV[4] laser, exciting the electronic states of the molecules, is used for solid MALDI.

The role of the matrix is to absorb the laser energy that leads to desorption. In this process the molecules are ejected with little aggregation and ionized.

1.2.1. Solid MALDI

We used different matrices for our samples, for example sinapinic acid for proteins, 2.5-dihydroxybenzoic acid for PEG samples and dithranol for polystyrene. The samples were previously dissolved in TFA, water and THF respectively, in a range of concentrations (for exact data, see [5]).

The applied voltages depended on the kind of detector, but were typically between 3 and 16 kV. More details can be found in [5].

1.2.2. Liquid MALDI

In contrast to solid MALDI, the molecules and the matrix are in a liquid phase. An IR laser[5], exciting the vibrational states of the matrix, gently desorbs the molecules. Liquid MALDI has three main advantages :

- the molecules are launched more gently with less heat-up and a narrower velocity distribution, leading to a better mass resolution ;
- many molecules are already in a liquid state, so the drying operation is avoided, thus reducing the damage probability ;
- the quantity of molecules and matrix supply, as well as the flow, can be precisely controlled from outside.

[4] Nitrogen laser provided by Laser Science Inc. : wavelength : 337 nm, pulse duration : 3 ns, energy per pulse : 300 µJ, spot size : 100 µm x 100 µm.

[5] A CO_2 laser from LSI : wavelength : 10.6 µm, pulse duration 150 ns, energy per pulse : 20 mJ, spot size : 200 µm x 200 µm.

In our setup, the analyte is introduced into the spectrometer via 96 micromachined nozzles Ø 4 µm, fabricated out of a silicon membrane [14]. One of them is shown in figure 1.2. Two Teflon tubes connect the outside to a reservoir located just behind the nozzles while syringes are used to control the pressure and the supply of liquid.

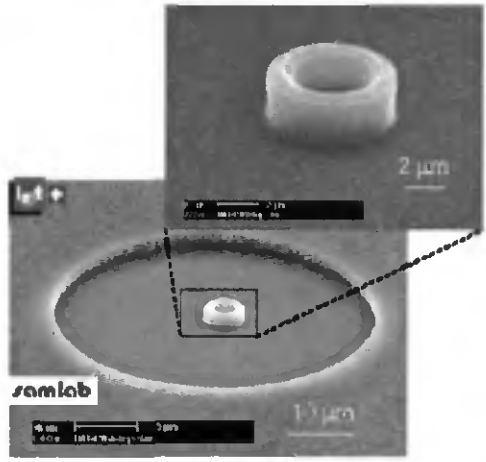

Fig. 1.2 : a SEM picture of one individual nozzle. The diameter of the aperture is 4 µm (from [14]).

One can easily control the quantity of liquid by imaging the droplet on a screen (a picture of the forming droplet is presented in figure 1.3).

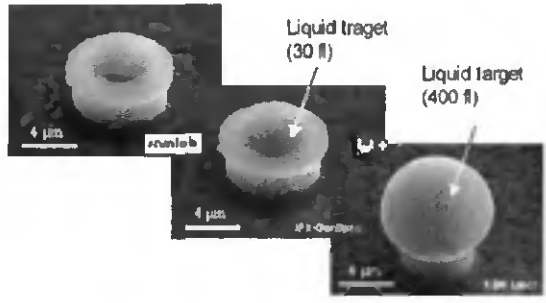

Fig. 1.3 : again SEM pictures of the formation of the droplet which has a maximum volume of 500 fl (from [14]).

1.3. Detectors

The last step consists of detecting the ions separated in time according to their m/q ratio. In classical devices, the detection is realized by an ion detector based on secondary electron multiplication. A classical ion detector is composed of several dynodes, each with a different potential. When an ion strikes the detection surface, one or more electrons are ejected. They are then accelerated to the next dynode, generating more electrons and so on, resulting, at the end of the cascade, in a measurable gain of 10^4 to 10^8. The discrete dynode configuration can sometimes be replaced by a continuous dynode. They are robust and have a large detection surface but they exhibit a rapid loss of sensitivity with slow molecules. The heavier the molecules are, the slower they travel for a given acceleration voltage. Thus the detectors become ineffective with masses weighing more than a few hundreds kDa. Several kinds of detectors have been developed to overcome this problem, the most promising being the cryodetector with a mass independent detection efficiency (see figure 1.4 and chapter 3 for an overview of cryogenic detectors).

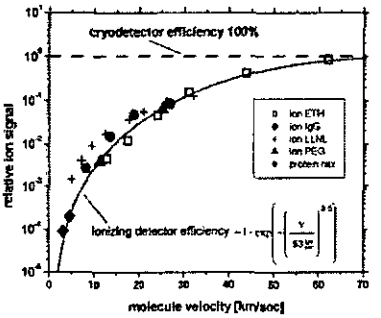

Fig. 1.4 : comparison of the efficiency between classic ionization and cryogenic detectors versus the molecule velocity. As it decreases exponentially with decreasing velocity for an ionization detector, the efficiency of the cryodetectors remains constant.

They were proposed for mass spectrometry in 1995 by Twerenbold [2]. Their detection mechanism is based on calorimetric properties.

1.4. Our experimental setup

As mentioned, we worked with both solid and liquid MALDI. The mass analyzer was a Time-of-Flight spectrometer and the detectors were superconducting tunnel junctions fabricated in our lab (see chapter 4). An overview of the whole setup is shown in figure 1.5.

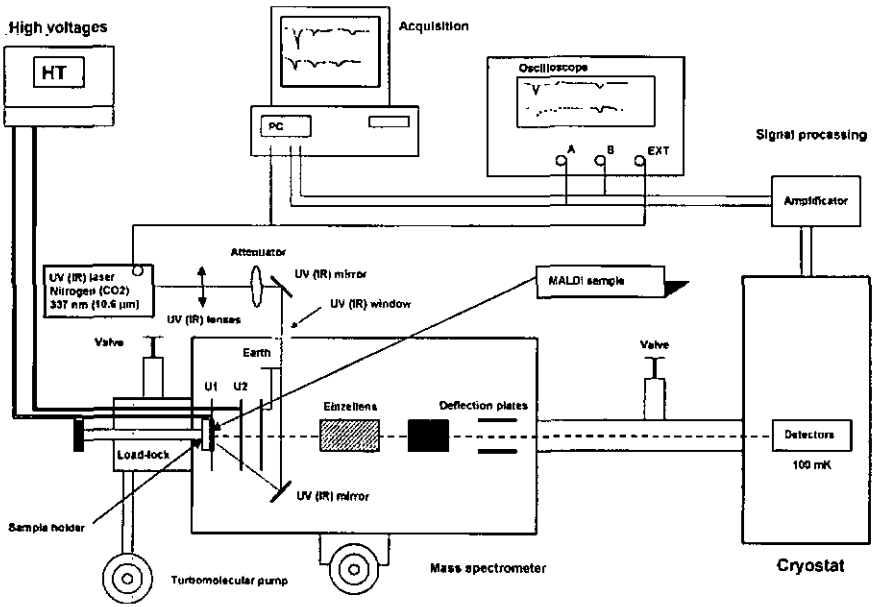

Figure 1.5 : schematic of the whole setup : at the left the ion source with the different devices, at the center the Time-of-Flight mass spectrometer and at the right the cryostat cooling the STJ down.

1.5. Spectra obtained with our previous array of STJ

The goal of this work was to develop further cryodetectors. Here we show for illustration results obtained previously in our lab with Al STJ. There were 5 STJ in-line, 100 µm-edged, diamond-shaped. They were fabricated with home-made masks and lift-off technique, tested in a little $^3He/^4He$ cryostat and cooled down in our dilution refrigerator. Some spectra are shown hereafter.

The first spectrum shown is that of insulin (m = 5'733 Da) (figure 1.6), prepared with a solid matrix, desorbed with a UV laser (voltages : 16 and 14 kV). This sample was prepared according to the recipe given in section 5.1.3. Our home-made spectrometer was coupled to the dilution refrigerator and two STJ were recording the data in parallel.

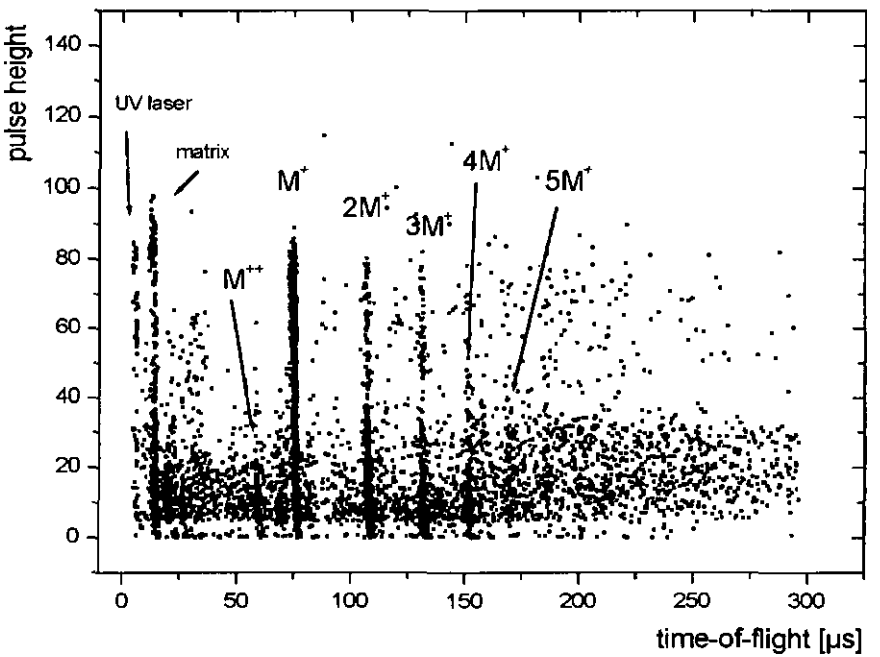

Fig. 1.6 : scatter plot of an insulin sample with sinapinic acid as matrix. We used a UV laser. Only one charge state is clearly visible.

As the second example, a spectrum of Bovine Serum Albumin (m = 66 kDa) is shown in figure 1.7. We used the same recipe to prepare the sample, the same setup, voltages and junctions.

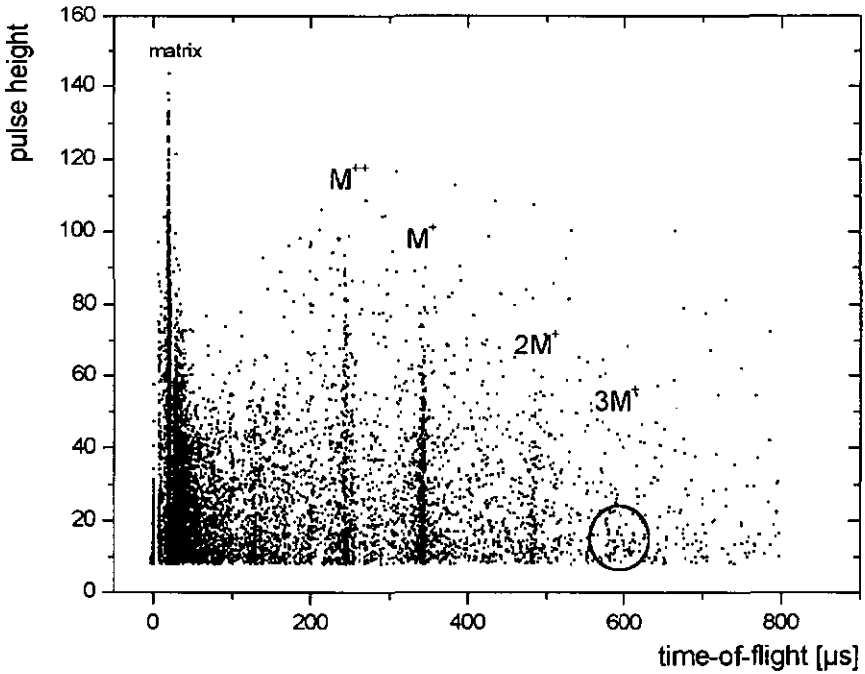

Fig. 1.7 : scatter plot of a BSA sample. One can notice the great M^{++} peak : this molecule is known to produce a lot of doubly charged molecules (peak at 240 µs).

Chapter 2

Superconductivity

Superconductivity is one of the most surprising behaviors of materials in physics. The vanishing of the dc-resistance is the best known effect but several other properties are worthy of interest, as described in this chapter.

2.1. Historical discoveries

In 1911, in Leiden, H. Kamerlingh Onnes was the first to discover the loss of resistivity of a metal below a given temperature (critical temperature T_c), namely mercury, three years after he succeeded in liquefying helium [15]. A few years later, in 1933, Meissner and Ochsenfeld observed that the magnetic field is expelled from all but a thin penetration depth near the surface of a superconducting material (a discovery which is now called « Meissner-Ochsenfeld effect ») (figure 2.1) [16]. As seen below, the flux lines of a magnetic field applied onto a superconductor are expelled outside.

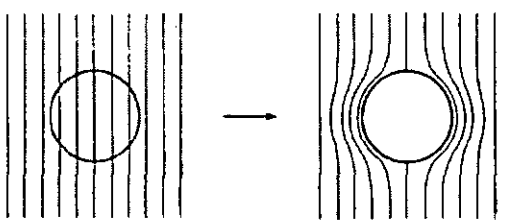

Fig. 2.1 : above T_c (a), the magnetic field passes through the material, it is expelled below T_c (b).

Two years after, H. and F. London developed a phenomenological theory of the electromagnetic properties of a superconductor [17, 18]. In 1950, Fröhlich made an important step by working on the ground state of a superconductor [19]. The same year, two independent groups showed that there was a transition temperature dependence with the isotope mass like $T_c \propto 1/\sqrt{m}$ [20, 21]. In 1953, Pippard introduced the « coherence length » (see 2.2.5.) and proposed a nonlocal generalization of the London equations [22]. In 1956, Cooper showed that some electrons near the Fermi level bind to form pairs, now called Cooper pairs [23]. J. Bardeen, L.N. Cooper and J.R. Schrieffer combined the previous ideas of Fröhlich and Cooper and developed their famous work, known as the **BCS** theory [24], which explains very well most of the superconducting effects.

2.2. BCS theory

2.2.1. Cooper pairs

In his model, Cooper explained that electrons in a pair have opposite wave vectors $\vec{k}$ and spin and are held together by virtual phonons [23]. The highest possible energy of those phonons is given by the Debye energy ($k_B \cdot \theta_D \approx 10meV$) and thus only the electrons near the Fermi surface can pair. The distance between them is called the "coherence length" (see 2.2.5.) and can be long. Because those pairs are bosons, hence do not suffer the Pauli exclusion principle, they obey Bose-Einstein statistics and thus are allowed to be in the same quantum state, which explains the zero dc-resistivity (the situation is different if an ac-current is applied).

The orbital Cooper pair wavefunction, i.e. the lowest energy orbital with total momentum equal to zero, is

$$\Psi_0(r_1, r_2) = \sum_k g_k e^{ik \cdot r_1} e^{-ik \cdot r_2} \tag{2.1}$$

where g_k are weighting coefficients.

2.2.2. BCS ground state

According to BCS theory [24], Cooper pairs condense until an equilibrium point is reached, when the binding energy for supplementary pairs is zero. A gap of forbidden energy Δ is created around the Fermi energy E_F. At T = 0, all and only the energy levels up to $E_F - \Delta$ are filled (see figure 2.2). At T > 0, the thermal phonons can break Cooper pairs, resulting in the creation of excited electrons, called quasiparticles, which fill the energy levels higher than $E_F + \Delta$.

The ground state of the BCS theory is

$$|\Psi_0\rangle = \sum_{k>k_F} g_k c^*_{k\uparrow} c^*_{-k\uparrow} |F\rangle \tag{2.2}$$

where $|F\rangle$ represents the Fermi sea with all states filled until k_F.

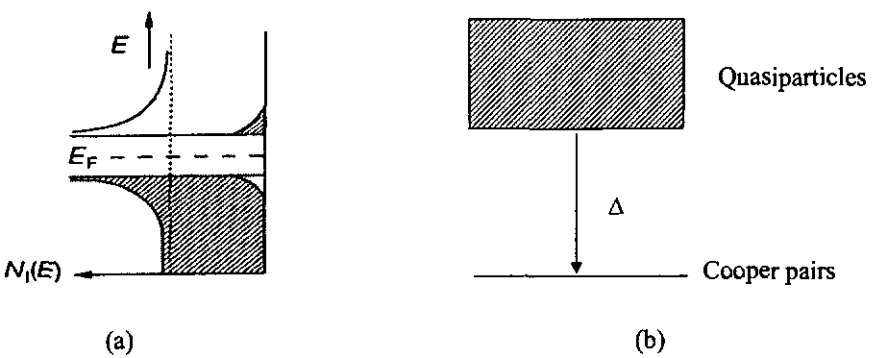

Fig. 2.2 : energy versus density of states for a superconducting material. One can note the gap Δ around the Fermi level and the thermally excited quasiparticles filling some of the energy levels above the gap. The Cooper pairs are on the Fermi level.

2.2.3. Determination of T_c

When the temperature approaches T_c, the gap tends to zero. At T = 0, the gap is of order of $k_B T_c$, more precisely

$$\frac{\Delta(0)}{k_B T_c} = 1.764 \tag{2.3}$$

2.2.4. Energy gap

The dependence of the gap with the temperature is shown in figure 2.3. It is noteworthy to notice that up to $T/T_c = 0.4$, the gap is almost constant and suddenly drops to zero at T_c with a tangent given by

$$\frac{\Delta(T)}{\Delta(0)} \approx 1.74\left(1-\frac{T}{T_c}\right)^{1/2} \tag{2.4}$$

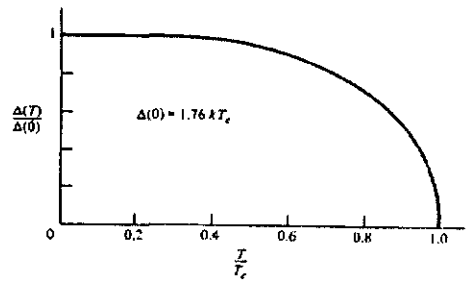

Fig. 2.3 : dependence of the gap with the temperature. The formula given in (2.4) is only valid when the curve drops to zero.

2.2.5. Coherence length

The coherence length is typically the distance between the two electrons of a Cooper pair. It can be deduced from Heisenberg's uncertainty principle :

$$\xi_0 \cong \frac{\hbar \cdot v_F}{2 \cdot \Delta} \tag{2.5}$$

where v_F is the Fermi velocity.

2.3. Additional properties of superconducting materials

London penetration depth

As mentioned on page 13, when a magnetic field is applied onto a superconductor, the magnetic flux lines are expelled outside the material, apart from a thin layer which is called « London penetration depth » and is dependent on the temperature :

$$\lambda_L \propto \left(1 - \frac{T}{T_c}\right)^{-1/2} \tag{2.6}$$

Note that the ratio between λ_L and ξ_0 is called the Ginzburg-Landau parameter and defines the type of the superconductor (I or II) which behaves in a different way when a magnetic field is applied (see [25] for more details).

Thermal properties

Thermal properties of normal and superconducting materials are given in section 3.1.

Tunneling effects

In 1962, Josephson noticed that the Cooper pairs could tunnel through a thin insulating barrier leading to a supercurrent. Bardeen did not agree and this situation gave way to a debate, related in [26]. More about tunneling is given in section 3.4.

Chapter 3

Cryogenic detectors

In many astrophysics and particle physics experiments, high sensitivity and energy resolution are required. Cryogenic detectors have the potential to fulfill these needs. The eighties have seen a rapid development of these novel kinds of detectors based on phenomena occurring at low temperatures, permitting resolutions never imaginable before. The energy gap in a superconducting detector (~ meV) is several hundred times smaller than in a semiconductor device : tbe charge induced by a particle of same energy is therefore hundreds of times greater.

There are many possible applications for these devices, from X-ray spectroscopy, dark matter search, X-ray astrophysics to materials science and mass spectrometry of biomolecules. Besides superconducting types of detectors, other families of cryodetectors are being developed. For a complete review on cryogenic detectors, see [27, 28]. The proceedings of « Low Temperature Detectors (LTD) » conferences give a complete overview of the development of the cryogenic detectors from the beginning until the latest results [29-37].

The present chapter is dedicated to the presentation in detail of the most common cryogenic detectors, grouped in three major families, i.e. thermal and fast thermal detectors, "transition" detectors and superconducting tunnel junctions, with an emphasis on the latter.

3.1. Thermal particle detectors

A thermal particle detector is a device which detects a particle interaction by measuring the temperature rise produced by the deposited energy. In the most simple model, the absorbed energy is fully thermalized and distributed among all possible excitation modes, leading to a temperature rise ΔT [38, 39].

More precisely the temperature rise $\Delta(T)$ is given by

$$\Delta T = \frac{E}{C(T)} e^{-\frac{t}{\tau}} \tag{3.1}$$

where $\tau = C(T)/G(T)$. $G(T)$ is the thermal conductance between the absorber and the heat sink at temperature T_0 (see figure 3.1) and $C(T)$ is the heat capacity of the absorber.

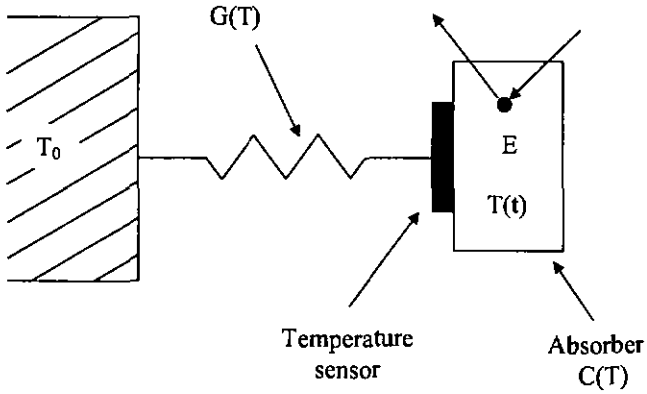

Figure 3.1 : a particle depositing its energy in an absorber of heat capacity $C(T)$ coupled by a weak thermal link of conductance $G(T)$ to a heat sink at T_0 produces a temperature rise of $\Delta(T) = T(t) - T_0$, measured with a temperature sensor *(see p. 22).*

Thus it is important to find absorbers with the lowest heat capacity so as to maximize the temperature rise for a given energy. Both electronic and lattice vibrations contribute to the total heat capacity of a material.

At low temperatures, the heat capacity of many materials becomes very small. This is especially true for pure dielectric crystals and superconductors, because their heat capacity decreases with the third power of the temperature, whereas it follows a proportional dependence in T for normal metals.

For a dielectric crystal, the heat capacity is dominated by the lattice specific heat :

$$C_{dielectric} = \beta \frac{m}{M} \left(\frac{T}{\Theta_D} \right)^3 \tag{3.2}$$

where $\beta = 1944$, m is the mass of the absorber, M its molecular weigbt and Θ_D the Debye temperature of the crystal. For a normal metal, the specific heat is dominated at low temperature by the electronic contribution which has a linear dependence with the temperature :

$$C_{normal} = \beta \frac{m}{M} \left(\frac{T}{\Theta_D} \right)^3 + c \cdot T \tag{3.3}$$

where c is a constant. For a superconductor, the lattice heat remains the same whereas the clectronic contribution decays exponentially with the temperature due to the exponential decrease of the quasiparticle density :

$$C_{sc} \approx \beta \frac{M}{M} \left(\frac{T}{\Theta_D} \right)^3 + a e^{-b\Delta / kT} \tag{3.4}$$

where a and b are materials constants.

Thus we can see that either dielectric or superconducting absorbers are suitable for cryogenic applications, having a T^3 temperature dependence.

Temperature sensors

To read the temperature T, two types of temperature sensors are described below : thermistors, which are doped semiconductors, and magnetic thermometers.

A thermistor is a heavily doped semiconductor which can either act itself as absorber, or be part of the absorber by doping a portion of it, or be a separate component glued onto the absorber. Doping can be achieved in several ways but the most common technique is neutron transmutation doping (NTD) : the semiconductor is exposed to a neutron flux, inducing transformation into isotopes of neighboring elements by neutron capture [40].

In general the resistivity vary as $T^{-1/2}$ in the region between 4 K and 10 mK. By measuring the resistance, one can have a precise value of the temperature.

Magnetic thermometers could in principle also be used but they encounter a problem because of the slowness of the heat transfer between the lattice and the thermometer, more precisely the spin system. In summary, the deposited energy induces spin flips and causes a change in the magnetic moment, measured with a SQUID.

3.1.1. Examples of thermal detectors

A few groups use different thermal detectors. In particular one can mention the Milano group which has been working for several years with such devices and was the first to perform underground experiments with them. Their main experiment is now called CUORE (Cryogenic **U**nderground **O**bservatory for **R**are **E**vents) : 1020 absorbers in TeO_2 5 x 5 x 5 cm will be assembled in 17 towers of 15 x 4 crystals each and cooled down to 10 mK. As temperature sensors, a NTD Ge thermistor will be glued on each crystal. One expects to improve the sensitivity to $\beta\beta0\nu$ and dark matter particles [41].

3.1.1.1. Transition Edge Sensors (TES)

Transition edge sensors differ somewhat in the concept. They were first developed by a Stanford group in 1990 [42]. A thin film of superconducting material (W, Ti, Al, etc) is deposited onto a substrate (typically a Si wafer). Then a meander is patterned whose continuous line is typically 2 μm wide, a few mm long and with 5 μm of pitch. The device is then current biased. When a particle interacts with the absorber, it creates phonons which drive a portion of the meander normal, producing a measurable voltage signal.

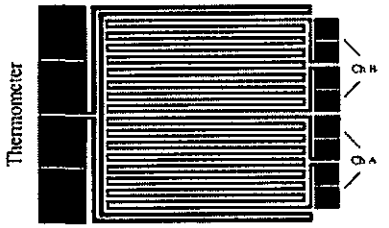

Figure 3.2 : TES fabricated by the Stanford group.

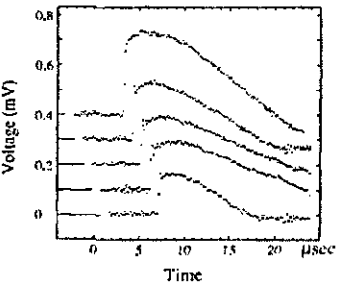

Figure 3.3 : pulses for 60 keV gamma rays.

3.2. Fast thermal detectors

Some small calorimeters are much more rapid than conventional thermal detectors, namely NIS junction detectors and electrothermal feedback TES.

3.2.1. NIS junction detector

A NIS junction is composed of a normal and a superconducting layers, separated by an insulation layer. The current is only flowing from the N part to the S part and is mainly dependent on the electron temperature of the N part[6]. When a particle interacts with the N absorber, the energy heats it up, producing a net current crossing the insulation barrier proportional to $1/T$. By carefully selecting the voltage bias, one can assure that only the "hotter" electrons tunnel [43, 44].

[6] Though NIS junction can be used as refrigerators (see, for instance, [44]).

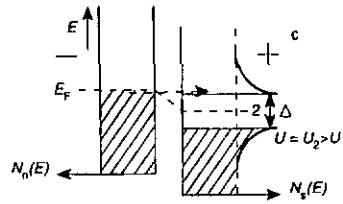

Figure 3.4 : biased NIS junction. One can see that a current can only flow from N to S part.

The NIST / Neuchâtel / GMU collaboration used a hot-electron microcalorimeter whose electron temperature sensor was a NIS junction [7].

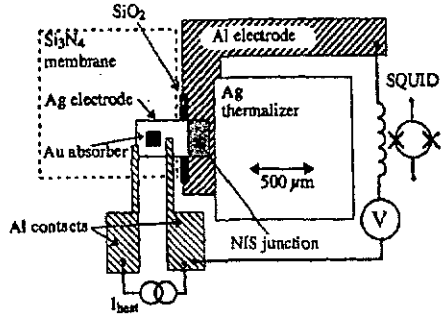

Figure 3.5 : NIS junction as detector : electrical circuit (from[45]).

3.2.2. Electrothermal feedback TES

The second device to be discussed in this section is the ETF-TES. The TES as temperature sensor was already overviewed (3.1.1.1.). Now, if the TES is voltage biased (V_B) and the temperature of the substrate is well below the transition temperature, the TES can self-regulate. After the hit of a particle, as the film cools down, its resistance drops to zero, thus increasing the Joule heating ΔI. Equilibrium is reached when Joule heating matches the heat loss into the substrate. The energy is thus given by

$$E = -V_B \int \Delta I dt \tag{3.5}$$

3.3. « Transition » detectors

3.3.1. Superconducting Strip Detector

This kind of detector was among the first to be used. The basic principle of operation is not complicated (see figure 3.6) : a thin and narrow strip of a superconducting material, deposited onto a substrate, is current biased just below its critical temperature. A particle hitting or passing through the strip leaves ionization energy creating a « hot spot » which turns a part of the strip normal producing a voltage signal. Thus there are some similarities with TES.

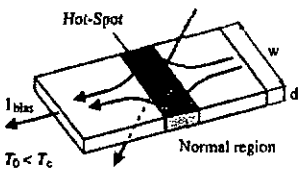

Figure 3.6 : a particle passing through the strip creates a « hot spot » driving a part of the strip normal, inducing a signal (from [28]).

3.3.2. Superconducting Superheated Granule Detector

Already in 1967, a group from Orsay (France) used superconducting superheated granules to investigate properties of the Ginzburg-Landau theory [46]. This kind of detector exploits the Meissner effect, explained in section 2.1. : granules of type I superconducting material of a few microns in diameter (figure 3.8), are placed in a static magnetic field and kept at a temperature T_s slightly below their critical temperature : the magnetic field is thus expelled from the interior of the granule. When a particle interacts with the granule, the deposited energy E will produce a temperature rise $\Delta(T)$ proportional to E (eq. 3.1). If T_s is chosen sufficiently close to T_c, the granule will be driven normal and the magnetic field will not be expelled anymore leading to a change of the configuration of the magnetic flux lines.

A pick-up loop surrounding the granule will feel a flux change $\Delta(\Phi)$ and produce a signal given by

$$\Delta V = \frac{\Delta \Phi}{\tau} \tag{3.6}$$

where τ is the flipping time between superconducting and normal state. Figure 3.7 shows what happens before an interaction and just after.

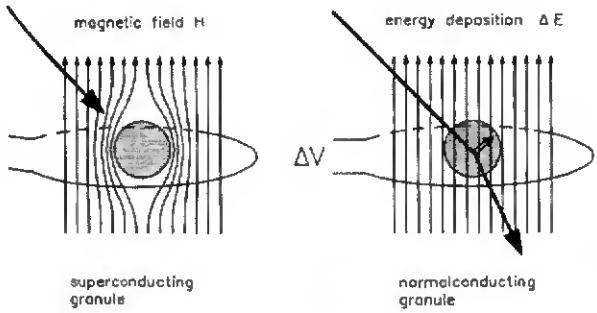

Figure 3.7 : principle of operation of a SSG (from [27]).

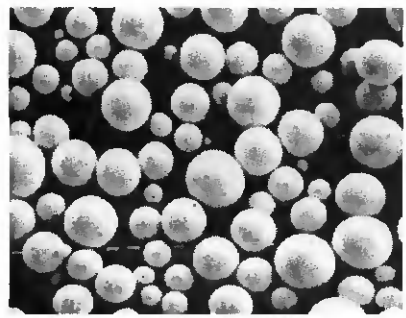

Figure 3.8 : picture of superconducting granules (from [47]).

This type of detector is presently used in the ORPHEUS experiment [48].

3.4. Superconducting Tunnel Junctions[7]

In its most simple expression, a superconducting tunnel junction (STJ) is made up of two superconducting layers, separated by an insulation layer, called a « barrier », which is typically 1 to 2 nm thick. This configuration is called "SIS" (Superconductor-Insulator-Superconductor). According to quantum mechanics, a particle has a non-zero probability to cross the barrier, even if its intrinsic energy is lower than the potential of the barrier. Already in 1932, experiments were performed with such devices but one had to wait until 1960 when Giaver published an important work on the current-voltage curve of a Al-AlO_x-Pb STJ [49, 50]. A few years later Sn/SnO_2/Sn junctions were used for the first time as nuclear radiation detector [51] and, in 1986, Twerenbold and Zehnder successfully detected X-rays with such tin junctions [52, 53, 54][8].

3.4.1. Tunneling processes

3.4.1.1. Normal tunneling in thermal equilibrium

An elcctron has a transmission probability to tunnel through a barrier of potential given by

$$P \approx \frac{16E_x}{U} e^{-\sqrt{8m^*(U-E_x)}\,l/\hbar} \tag{3.7}$$

where $E_x = \hbar^2 k^2 / 2m^*$ is the kinetic energy of the electron, U the potential barrier height and l its width (see figure 3.9) [55]. Thus the tunnel rate is simply the number of hits against the barrier times the transmission probability :

$$R = \frac{v_x}{2d_1} P \tag{3.8}$$

where v_x is the electron-group velocity in the x-direction and d_1 the thickness of the electrode 1.

[7] More details on different types of STJ can be found in [56-63].
[8] A complete description of the tunneling and its applications is given in [64].

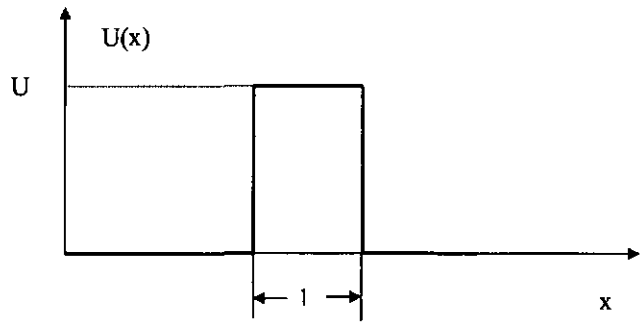

Figure 3.9 : scheme of a simple potential barrier, comparable to a tunneling barrier.

For low voltages, the tunneling current is described by

$$I = 2eN(0)AdW \int_{-\infty}^{\infty} [f(E) - f(E - eV)]dE \tag{3.9}$$

where A is the area of the barrier, $N(0)$ the density of states at the Fermi level and V the voltage across the junction.

3.4.1.2. Superconducting tunneling in thermal equilibrium

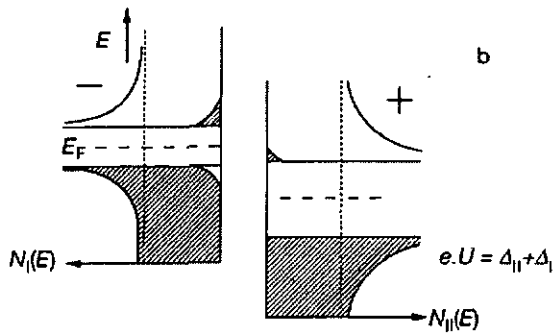

Fig. 3.10 : density of states for two different biased superconductors forming a STJ.

When a SIS junction is cooled below its critical temperature (T_c), either Cooper pairs or quasiparticles can tunnel, the former leading to a current, called "dc Josephson current" (see section 3.4.3.). At T = 0, the latter does not exist because the electrons are all condensed into Copper pairs. At T > 0, thermal phonons can break up pairs into quasiparticles, which can, in principle, tunnel if the two films are from different superconducting materials. If they are from the same metal, a voltage applied across the junction will allow quasiparticles to tunnel. Note that the population of thermal phonons, able to create quasiparticles, decreases exponentially with decreasing temperature, as shown in figure 3.11.

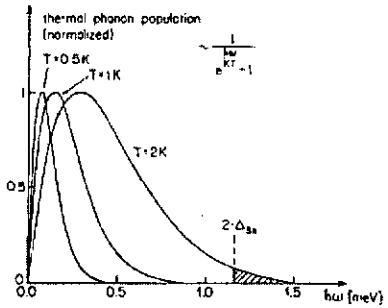

Figure 3.11 : thermal phonon population versus energy for different temperatures (the minimum energy to break a Cooper pair in tin is $2 \cdot \Delta_{sn}$) (from [65]).

There are four ways to transfer an electron charge from one film to another (see figure 3.12), each one creating a current. The back-tunneling can lead to an amplification mechanism called "Gray effect" [66].

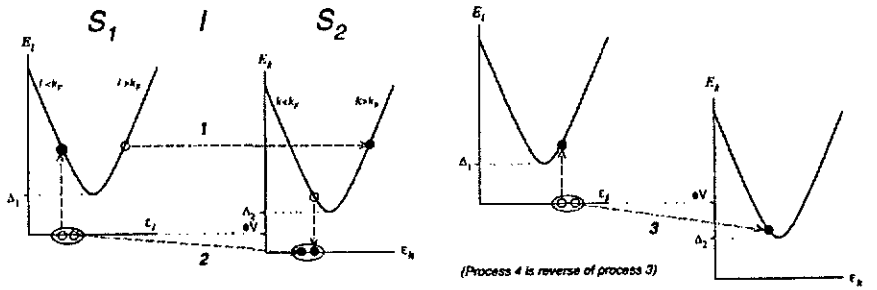

Figure 3.12 : the four tunneling processes (from [55]).

For a bias voltage $\frac{k_B T}{e} << V < \frac{2\Delta}{e}$, the current resulting from the four processes is proportional to $N_{th} \cdot \tau_{tun}$, where $N_{th} \approx \sqrt{T} \cdot e^{-\Delta / k_B T}$ is the density of quasiparticles and τ_{tun} the tunneling time given by

$$\tau_{tun} = R_N e^2 N_n(E_F) S d \tag{3.10}$$

where R_N is the normal resistance of the junction (see section 3.4.2.), $N_n(E_F)$ the density of states, S the area of overlap of the two films and d the thickness of the barrier. But not all the quasiparticles tunnel because some of them recombine into Cooper pairs with a rate of

$$\tau_{rec}^{-1} = \alpha \sqrt{T} \cdot e^{-\Delta / k_B T} \tag{3.11}$$

In this case, the STJ can be run as a temperature sensor, the tunnel current being proportional to T.

3.4.2. Current-voltage curve characteristics

One of the most important characteristics of a STJ is the current-voltage curve, named hereafter I-V curve. Figure 3.13 shows a typical curve for a $Sn/SnO_x/Sn$ junction.

One can roughly distinguish two regions : the subgap region for $V < 2\Delta / e$ and the normal region where $V > 2\Delta / e$. At T > 0, when a small bias is applied, the quasiparticles can tunnel. The current remains constant until V reaches $2\Delta / e$: then the two quasiparticles forming a Cooper pair can suddenly break up, leading to a very strong current. For higher voltages, the normal electrons can tunnel, giving rise to an ohmic slope. This phenomenon occurs at $V = (\Delta_1 + \Delta_2)/e$ for two different superconducting materials with gaps Δ_1 and Δ_2.

Thus we can define two different resistances : R_N, the normal resistance of the above-mentioned ohmic slope and $R_D = \partial U / \partial I$, the dynamical resistance measured at the bias point (δi of figure 3.13) (see section 3.4.4.).

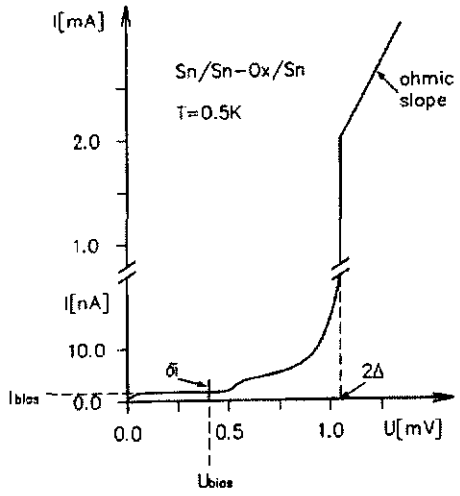

Fig. 3.13 : typical I-V curve for a tin junction (from [27]).

3.4.3. DC Josephson current[9]

At any time, the Cooper pairs can tunnel. Because they are bosons, they encounter no resistance, hence leading to a vertical trace on the I-V curve [67]. One can suppress it by applying a magnetic field orthogonally to the STJ (figure 3.14).

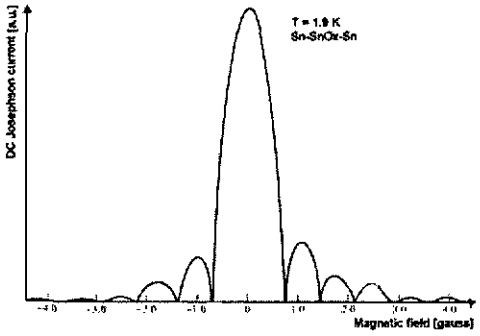

Fig. 3.14 : suppression of the DC Josephson current versus applied magnetic field.

[9] AC Josephson effect also exists, see [68, 69].

3.4.4. STJ as particle or X-ray detectors

This is the type of detector used in this work. When a photon or a particle interacts with one of the films, it produces phonons, via the photoelectric effect, which can break Cooper pairs, creating a quasiparticle excess. If they tunnel before recombining, they will produce a measurable signal, i.e. the collected charge will be :

$$Q_{coll} = Q_0 \frac{\tau_{tun}^{-1}}{\tau_{tun}^{-1} + \tau_{rec}^{-1} + \tau_{misc}^{-1}} \qquad (3.12)$$

where τ_{tun} and τ_{rec} are the tunneling and recombination times seen in section 3.4.1.2. and τ_{misc} includes geometric effects and phonon losses in the substrate [70].

It is important that $\tau_{tun} \ll \tau_{rec}$; therefore, one has to work at very low temperature (usually $T \approx T_c/10$), since the recombination time depends on the temperature (eq. 3.11).

We usually bias the junction at $V = \Delta/e$. R_D measured at this point should be at least a few kΩ to match the impedance of the FET preamplifier, whereas R_N should not be higher than a few Ω, in order not to prevent the tunneling (eq. 3.10).

As seen before, an X-ray or a particle can interact with either top or bottom film, leading surprisingly to a current with the same sign (see figure 3.15).

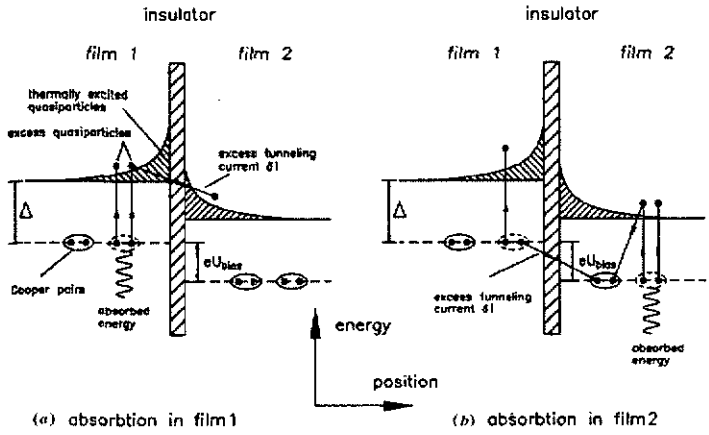

Fig. 3.15 : absorption processes into top and bottom films : both currents have the same sign (from [27]).

Chapter 4

Experimental setup

Our experimental apparatus consists of a MALDI-TOF mass spectrometer, coupled to a dilution refrigerator or an ADR containing the detectors, the STJ in this case. A base pressure of 10^{-7} mbar is maintained in the apparatus by a turbopump backed by a rotary pump. A schematic of the whole assembly is given in figure 4.1. The sample to be analyzed is introduced into the mass spectrometer either with a syringe (as in figure 4.1) or predeposited upon a sample holder. In the first case, the growth of the droplet is monitored by use of a camera. The molecules are then desorbed by a short laser pulse, accelerated towards the detector through the spectrometer, enter the dilution fridge through the side-access port and hit the detector, producing a current signal which is amplified and recorded.

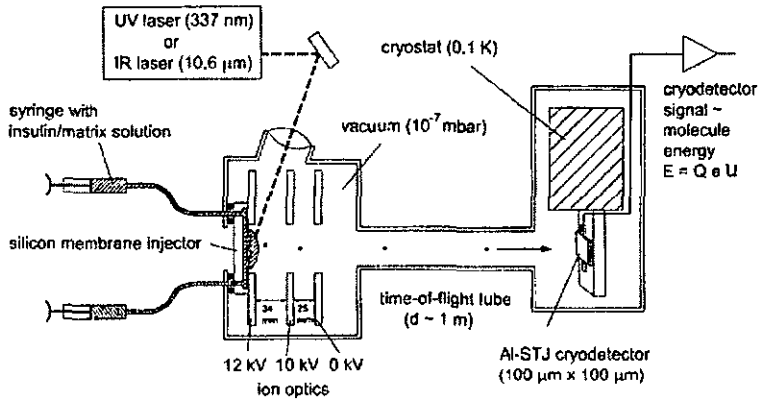

Fig. 4.1 : schematic of our experiment, in this case using liquid MALDI technique (from [71]).

Section 4.1. describes the fabrication of the STJ on different substrates while chapter 4.3. treats the subject of acquisition electronics. The cryogenics we use is described in section 4.2. and mass spectrometry in 4.4.

4.1. STJ fabrication

My main fabrication task during this thesis was to develop an array of $Al/AlO_x/Al$ STJ detectors. We designed an array of 16 STJ in line (easy to fabricate with a shadow-mask technique), 100 µm side-length (good compromise between noise and surface detection), diamond-shaped (a simple and good design to suppress the Josephson current), separated by 72 µm (owing to constraints on our deposition area).

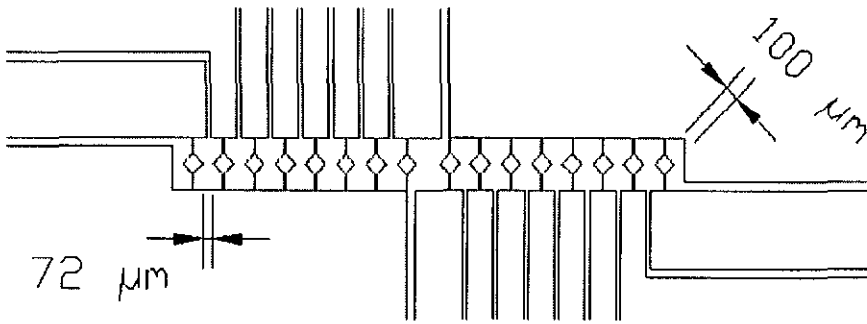

Fig. 4.2 : design of the 16 STJ array, divided in two groups of 8 junctions. Each group, separated by 160 µm, has its own common point.

Two different processing routes (lift-off and etching) and three different substrate types were investigated. In general, the fabrication procedure was as follows :

1) preparation of the substrate ;

2) evaporation, photolithography (conversely for lift-off) and cleaning ;

3) mounting and bonding.

Those three stages are explained more in details in section 4.1.1. to 4.1.3.

4.1.1. Substrates

I deposited the 16 STJ array onto three different substrate types : glass, polyimide and gallium arsenide. They all need different preparation, as described in the next sections.

4.1.1.1. Glass substrate

Glass is an amorphous material. One thus almost completely avoids the « substrate events » created by a phonon coming from the substrate, because the phonon propagation is strongly reduced in an amorphous structure. Glass was then the first material to be used for our experiments. It was 18 x 18 mm and 0.15 mm thick, supplied by Merck.

Before evaporation, the substrate was cleaned in acetone with a cotton bud, rinsed with isopropyl alcohol and dried with pure nitrogen.

4.1.1.2. Polyimide substrate

The STJ are heated up by the laser pulse, thereby increasing the thermal subgap current and reducing the signal-to-noise ratio of the device. Glass has poor thermal conductivity, so I developed a substrate consisting of a copper disc on which a 1.5 µm thick layer of dielectric polyimide was applied by spinning. This enables the junction to cool down more rapidly after the laser pulse, reducing the relaxation time of the device [72].

The copper disc was Ø 25 mm and 1.5 mm thick. Both faces were diamond milled before being cleaned in an ultrasound bath containing first acetone then isopropyl alcohol. Then the upper face was optically polished and cleaned again with the same solvents.

To increase the adherence of the polyimide film on the copper disc, an adherence promotor (HDMicrosystems VM-651) was dispensed on the substrate, spun and baked at 120° C for 1 minute. The liquid polyimide PI 2555 from HDMicrosystems was then dispensed with a pipette, spun at 5'000 RPM and baked on a hotplate at 120° C and 150° C, in each case for 30 seconds. Then it was cured in an oven, following a precise heating and cooling procedure : heating from room temperature to 200° C with a rate of 4° C per minute, 30 minutes at 200° C, again heating from 200° to 300° C (rate : 2.5° C / min), 1 hour at 300° C and gradual cooling to room temperature.

4.1.1.3. GaAs substrate

The idea of filtering the phonons is not new [73], but to use this technique to increase the signal-to-noise ratio of STJ acting as a macromolecule detectors is something which had not been undertaken yet. Our idea was to build a substrate which reflects the high-energy phonons created by the impact but which is transparent to the low-energetic thermal phonons. Thus we hoped to increase the gain by losing less phonons into the substrate.

We deposited hundreds of GaAs/AlAs layers alternatively becoming thinner and thinner, acting as filter, on a 400 µm gallium arsenide wafer, then a 2 µm thick GaAs layer as dielectric. All those layers were grown in the MBE of Prof. Faist's group in Neuchâtel. The configuration of the sample is shown in figure 4.3.

Fig. 4.3 : TEM (Transmission Electron Microscope) micrograph of one of our samples : one can see the alternation of GaAs and AlAs layers, being from 34 Å to 7 Å thick. A dielectric layer of GaAs is then deposited onto the layer stack.

Simulations of reflectivity versus energy of the phonon have been made for different angles, 90° being normal to the surface and 0° parallel. As shown in figure 4.4 (for an incident angle of 50°), reflectivity of phonons with an energy greater than 0.4 meV is excellent, for angles from 90° to 40°. Lower, the reflectivity fluctuates too much to consider the stack as a filter.

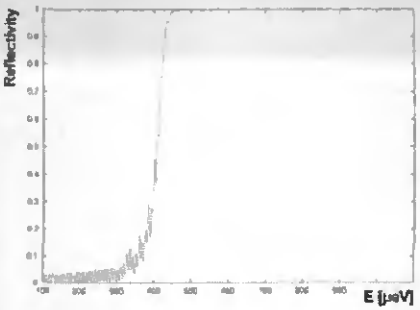

Fig. 4.4 : reflectivity of the phonons versus their energy for a incident angle of 50° (90° being narmal to the surface of the sample).

Before evaporating the STJ, the substrate was cleaned with isopropyl alcohol and dried with pure nitrogen gas.

4.1.2. Fabrication

Two techniques have been used to fabricate the array, etching and lift-off[10]. However, the former proved to be more reproducible and all the detectors used for this work were fabricated by this method. The main advantage of etching is to oxidize the edges of the junctions, allowing them to have a longer life cycle without leaks. It is also easier than lift-off to remove the remanent metal because the film is not floating on a temporary layer. In both cases, the aluminum was deposited using the shadow-mask technique, explained in the captions of figures 4.5 and 4.6. Note that the maximum of the surface remains covered with the aluminum in order to have the maximal thermal reflectivity.

The following codes are used to define the different layers in the two next pictures :

Substrate | Al film | Oxide layer | Overlap of the two films | Resin | Optical mask

[10] More details are given in reference [74].

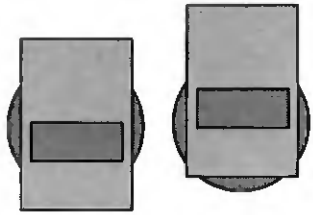

The first layer is evaporated and oxidized, then the mechanical mask is shifted and the second layer is evaporated.

A cut of the two films. The overlap is where the STJ are going to be.

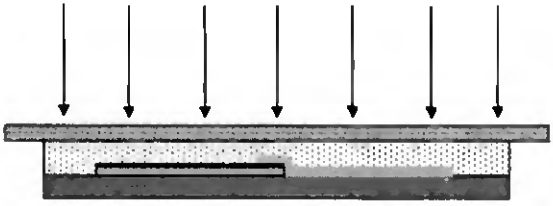

A thin layer of resin is spun, then the STJ and pads are defined under UV light.

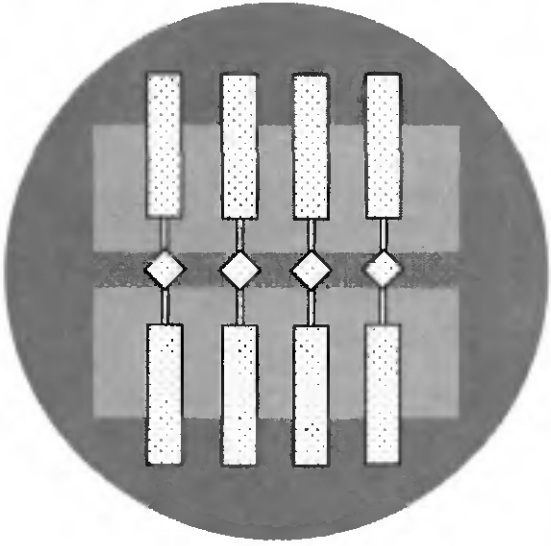

The resin is now developed around the future junctions. Then the substrate is plunged into an acid bath and the metal which is not protected by the resin is dissolved.

Fig. 4.5 : schematic of the etching process we preformed.

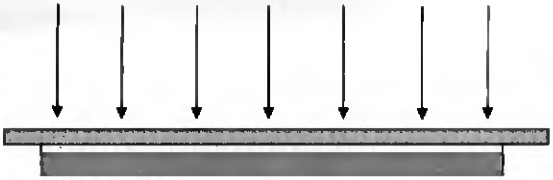

The resin is spun onto the substrate and exposed under UV-light (a contact mask is used to define the structure).

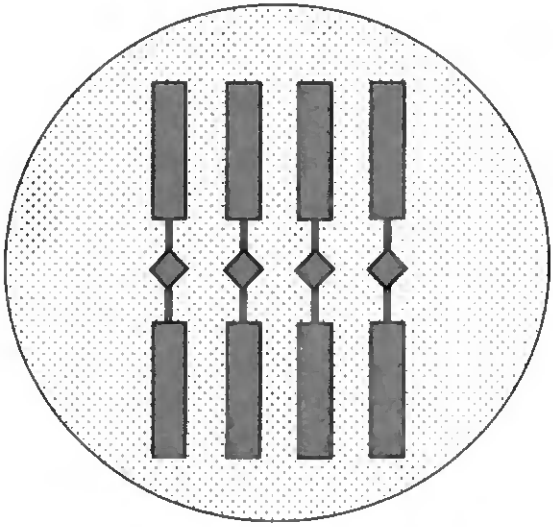

The resin is then developed and the irradiated parts are dissolved.

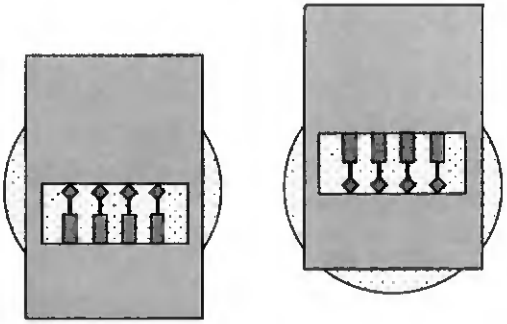

The first layer of aluminum is then evaporated with the mask in position as on the left picture and oxidized. The mask is shifted as on the right and the second film deposited.

Fig. 4.6 : schematic of the lift-off process.

4.1.2.1. Etching

The process is illustrated in figure 4.5. The substrate is mounted, together with the shadow-mask in its first position, onto an appropriate sample bolder and put into vacuum. After a few hours of pumping with a 1000 l/s turbomolecular pump, the pressure reaches 10^{-10} mbar ; the first aluminum film (200 nm) is then electron-beam evaporated [75] with a rate of 10 Å/s. Afterwards, the sample is transferred into the load-lock and kept under a pressure of 3 mbar of pure oxygen for 30 minutes. This will create the Al_2O_3 insulation barrier, about 10 Å thick. Then the load-lock is pumped to a pressure of $5 \cdot 10^{-7}$ mbar, the mask is mechanically shifted to the other side (without breaking vacuum) and the sample holder is brought back into the main chamber where the second film is evaporated, first at 2 Å/s for 5 nm, in order not to risk damaging the fragile barrier, then 5 Å/s until 15 nm and finally the rest at 10 Å/s (total thickness 150 nm).

The next step is to pattern the « sandwich » of aluminum films. A 3 µm photoresist layer (Shipley 3008) is spun onto the sample at 3'000 RPM for 40 s. The resin is then exposed under UV light (i-line 280 nm) for 7 seconds with the suitable mask and developed for 1 minute (Megaposit Developer 1 : 1 H_20 deionized). After being dried with nitrogen, it is plunged into a mixture of acids (HNO_3 1 : 8 H_3PO_4), heated at 50° C, for 25 s. Finally the sample was rinsed in analytic-grade acetone to remove the remanent photoresist.

4.1.2.2. Lift-off

Here the junction deposition process is the same but it takes place onto a substrate on which the photoresist is already patterned (see figure 4.6). Afterwards the photoresist is dissolved in acetone and undesired metal floats off. As for etching, a photomask and a mobile shadow-mask are required for junction definition.

The sample is put on the sample holder and the shadow-mask, in its first position, is aligned with the photoresist pattern under a microscope. The sample holder is transferred into the evaporation chamber where the two films are deposited and oxidized, according to the recipe described in the previous section. Afterwards the sample is soaked in analytic-grade acetone to get rid of the resin and the undesired metal, rinsed in analytic-grade isopropyl alcohol and dried.

The greatest problem with this technique is to have a very sharp-edged photoresist pattern, in order to make a clear separation between the metal deposited onto the substrate and onto the resin. Otherwise the layer is not discontinuous, leading to ripped junctions edges which can affect the resolution or even destroy the structure when removing the resin.

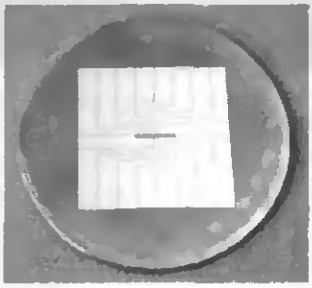

Fig. 4.7 : 16 STJ on a polyimide substrate ready to be mounted. There is one common point per 8 STJ.

4.1.3. Mounting

The samples were then mounted on a copper sample holder and clamped in place with either a printed circuit board (PCB) or a copper piece. The pads were bonded to the PCB, on which a connector was soldered (see figure 4.8).

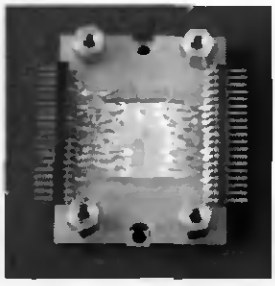

Fig. 4.8 : picture of on array that we fabricated on a glass substrate. The 90°-bent connectors at both sides are soldered onto the copper pads of the PCB. A 45 μm Al wire connects the copper pads to the STJ pads. The copper hexagonal screws hold the assembly and the thermal shield, which supports the ^{55}Fe source.

4.2. Cryogenics

Three cryostats were used in our research : a $^3He/^4He$ cryostat, made to test our junctions, a dilution refrigerator, equipped with a side-access arm, to make measurements with macromolecules and an ADR cryostat, also with a side-access tube. They are described in the three next sections. Complete methods and techniques used in cryogenics are well described in [76, 77].

4.2.1. $^3He/^4He$ cryostat

We have at our disposal a custom-made $^3He/^4He$ cryostat, operating in the « single-shot » mode, with a base temperature of 300 mK.

The insert is first cooled in liquid nitrogen, then with L^4He, on which we pump afterwards to reach 1.2 K, below the liquefaction temperature of ^3He. Pumping on the ^3He permits us to cool down to 300 mK. The entire process takes only four hours.

Five channels are available in this cryostat. Each one possesses its own preamplifier (Icarus_B) and can be individually biased. An electric shock can also be applied in order to eliminate the trapped magnetic flux. External Helmholtz coils produce the magnetic field to suppress the DC Josephson current. Details on electronics are given in section 4.3.

From the I-V curve, one measures the values of the thermal plateau, the gap, the Josephson current, the dynamic and the normal resistances (R_D and R_N) (see section 5.1.1.). Finally, an X-ray spectrum is recorded to check if the detectors work properly. The X-ray source is a ^{55}Fe source[11].

4.2.2. Dilution refrigerator

The Oxford Instruments Kelvinox 25 dilution refrigerator has a cooling power of 25 μW and a base temperature of 31 mK. This cryostat was modified by including a side-access arm, allowing the macromolecules to reach the detector. As a result of this, the base temperature of the mixing chamber degraded to 80 mK, due to the infrared radiation coming from the spectrometer. The side-access is made of three concentric copper shields to reduce thermal radiation. In addition, the apertures

[11] The two main lines are K_α = 5.89 keV and K_β = 6.49 keV.

which allow the flight of the molecules through the system are only 5 mm in diameter.

19 coaxial cables were used to connect the STJ to the preamplifier box. The exact connecting and amplifying schemes are explained in section 4.3.

4.2.3. Adiabatic Demagnetization Refrigerator (ADR)

The third cryostat is an ADR from Janis Research Instruments. The two stages with different salts (FAA et GGG) permit 80 mK to be reached. This cryostat is also equipped with a side-access arm. The magnetization process lasts about two hours (ramping from 0 to 9 amperes), whereas the ramping down takes one hour. One can work more than five hours before having to cycle again. Most of the results with STJ on polyimide substrate were obtained with this cryostat.

4.3. Electronics

This section describes the electronic circuit from the STJ to the personal computer and the analysis programs.

4.3.1. General scheme

The readout scheme is composed of three main parts :

1) the wiring ;

2) the amplification stages ;

3) the acquisition process.

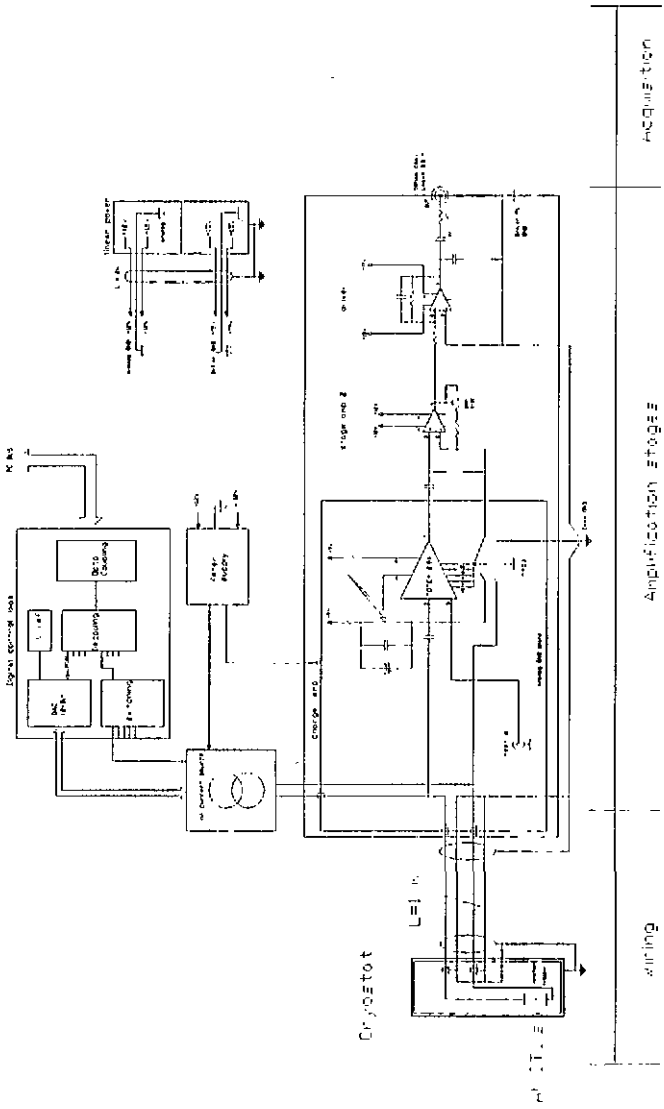

Fig. 4.9 : schematic of the general electronic circuit, divided in three parts : the wiring from the STJ to the amplifiers, the amplification part and finally the acquisition system.

4.3.2. Wiring

Our three cryostats were home-wired. For the dilution and the ADR, we used phosphor bronze non-magnetic wire (NM-36 AWG Ø 0.127 mm, supplied by LakeShore). The insulation is made of polyvinal formal (Formvar), a material with excellent mechanical properties, such as flexibility or abrasion resistance. The electrical conductivity of such a wire is $1.15 \cdot 10^{-7} \Omega m$ at 293 K. Before being installed, they were manually twisted in order to reduce the magnetic field effect. The ^{3}Hc/^{4}He cryostat is wired with Constantan.

One wire of the twisted pair connects the signal from the STJ, the second is grounded. Each junction is connected to a common point wired by one twisted pair.

4.3.3. Amplification stages

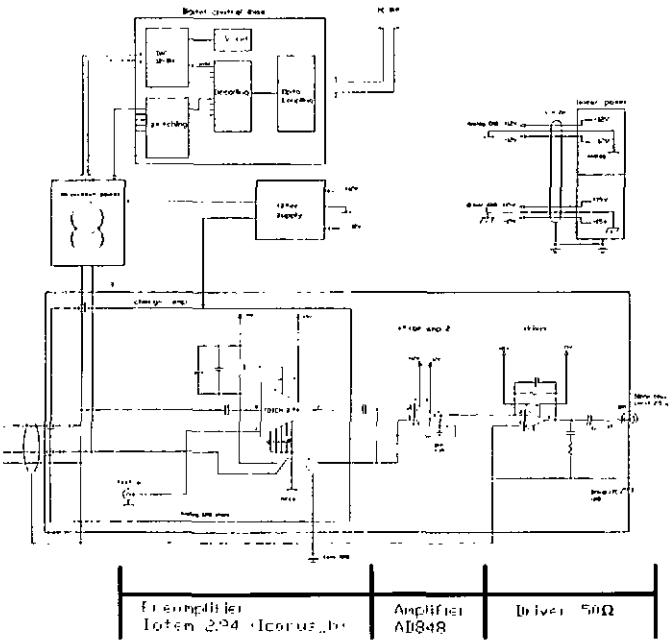

Fig. 4.10 : electronic scheme of the amplification stages.

The junctions are current-biased. The signal is amplified by a charge-sensitive preamplifier Totem 2.94 (Icarus_B) and by an operational amplifier AD848. A 50 Ω active driver matches the impedance of the cables. All these components, as well as the current source, are enclosed in a metallic box. One can also apply a shock onto the junction (typically 5 mA) to remove the trapped magnetic flux.

Connectors are generally made by Lemo[12], except those for the dilution refrigerator where SMA connectors[13] were used.

4.3.4. Acquisition

The acquisition is assured by a personal computer via Gage cards on which the sampling rate can be chosen between 1 to 20 MHz. The acquisition program records every event in energy versus time-of-flight. Number of acquired channels, pre-trigger and post-trigger times, trigger level, trigger slope and sample rate can be directly selected. When the acquisition is over, a home-made program searches for peaks and a third one is used to visualize either the scatter plot or the histogram.

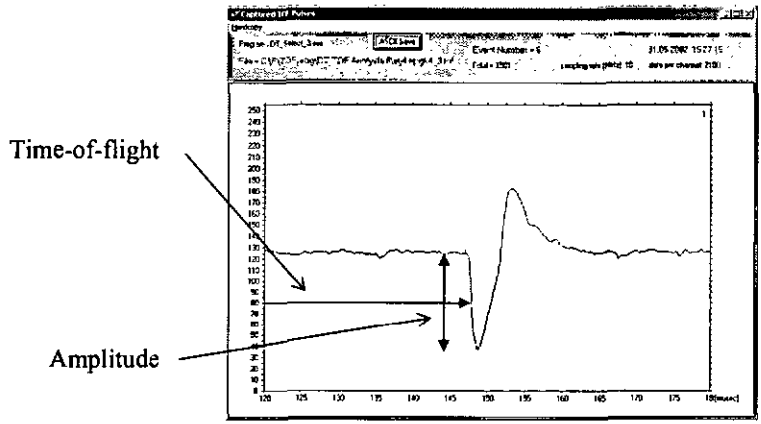

Fig. 4.11 : a typical pulse induced by a molecule and the two parameters extracted to create a scatter plot of energy versus time-of-flight.

[12] More informations on Lemo connectors on : « http://www.lemo.com ».
[13] All types described on : « http://www.hyperlinktech.com/web/connectors_sma.html ».

4.4. Mass spectrometry

We manufactured two identical spectrometers, one for liquid and one for solid MALDI. The pressure inside reaches $5 \cdot 10^{-7}$ mbar thanks to a turbomolecular pump and a liquid nitrogen trap. Two high-voltage supplies are used for the electrodes, an *Einzellens* is used to focus the beam and two deflection plates can deviate it or filter out undesired elements.

A load-lock, evacuated by a separate pumping station, permits the sample to be introduced under vacuum. A CCD camera is used to monitor the position of the laser spot on the sample holder. The spot can be moved over the whole surface of the sample by slightly displacing the laser with high-precision micrometric screws. An attenuator, a mirror and a lens, all on an optical bench, complete the set of tools we have to focus and adapt the beam.

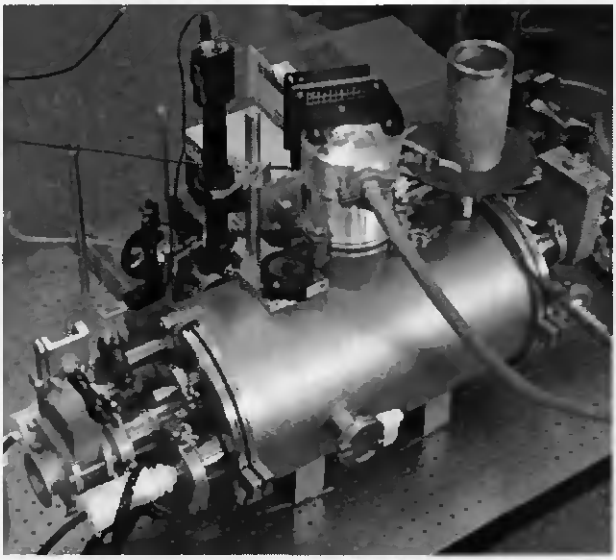

Fig. 4.12 : picture of one of our spectrometers, equipped with a UV loser (solid MALDI). The cryostat is located at the right side of the image. The load-lock used to introduce the sample with a rod is connected to the valve at the left part of the spectrometer.

For each of the macromolecules to be analyzed, the way of preparing the sample is different. Precise recipes are mentioned in the text for individual cases. However, the matrices we used are listed below.

Solid :	proteins	:	Insulin	(5'733 Da)	: sinapinic acid
			Lyzozyme	(14'300 Da)	: sinapinic acid
			BSA	(66'000 Da)	: sinapinic acid
			IgG	(130'000 Da)	: sinapinic acid
			Hpgk4	(9'695 Da)	: sinapinic acid
Liquid :	proteins	:	Insulin	(5'733 Da)	: glycerol

We got them from :

Insulin		: Sigma	I-5500
Lyzozyme		: Sigma	L-7001
BSA	(Bovine Serum Albumin)	: Sigma	B-2518
IgG	(Immunoglobulin type G)	: Sigma	M-8642
Sinapinic acid		: Fluka	85430
Glycerol		: Aldrich	19,161-2
Dimethylsulfoxyde (DMSO)		: Aldrich	49,442-9
Tetrafluoracetic acid (TFA)		: Aldrich	29,953-7
Ethanol		: Merck	1.00983.1000
Water for chromatography		: Merck	1.15333.30064

Chapter 5

Experimental results

This section is divided into two parts : the first section describes the results obtained with STJ on polyimide substrates and the comparison between the latter and STJ on glass substrates. In the second part, we present some comments about energy transfer when an X-ray or a macromolecule interacts with a STJ (either with Ta or Al STJ).

5.1. Results with polyimide substrates

When using lasers with relatively high power, e.g. the 10 μm IR laser we used, the reflected light onto the sample holder heats the STJ. The pulse height distribution of the STJ signals shows a nonlinear increase for larger time-of-flight values owing to cooling of the STJ after the large heating effect of the laser. When the temperature decreases, the recombination rate also decreases and more charges will be collected, according to equations 3.11 and 3.12. The junction needs a certain time to cool down and to retrieve its full capability of detection. When using STJ as a detector, the signal of the molecules prior to the complete thermal recovery is smaller. This fact is clearly visible in the figure 5.10.

The goal of using polyimide substrates was to increase the thermal recovery rate of the STJ after a laser pulse. By improving the thermal link between the junction and the cold finger, this effect is minimized. Thus the more the STJ are thermalized, the shorter the recovery time is.

To increase the cooling rate after a heat pulse, we proposed depositing our array on a material with good thermal conductivity, e.g. on copper. To electrically insulate the junctions, a polyimide layer, 1.5 μm thick, was deposited onto the copper disc : this layer acts in fact as the substrate.

Al STJ were fabricated on a polyimide-coated copper disc, according to the procedures described in sections 4.1.2.1. (wet-etching technique). The disc was pinched between the sample holder and a squeezing piece, also in copper, as shown in figure 5.1.

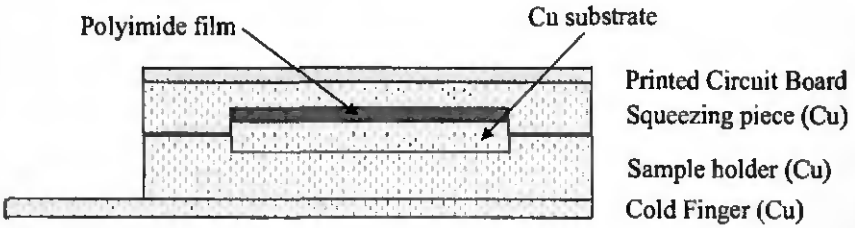

Fig. 5.1 : schematic of the assembly designed to be mounted in all our cryostats.

This design was chosen in order to maximize the thermal link between the copper disc, i.e. the STJ, and the cold finger.

5.1.1. I-V curves

The STJ were cooled down in our ADR cryostat to 81 mK and the I-V curves were measured. A typical example is shown in figure 5.2.

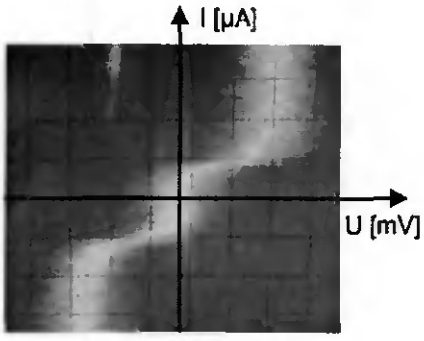

Fig. 5.2 : I-V curve of our new Al STJ on polyimide substrate. 1 vertical division is 1 μA.

A plot of this curve is shown in figure 5.3. This is not to scale because the image was reduced. Note that there is a gain of 50 on the voltage.

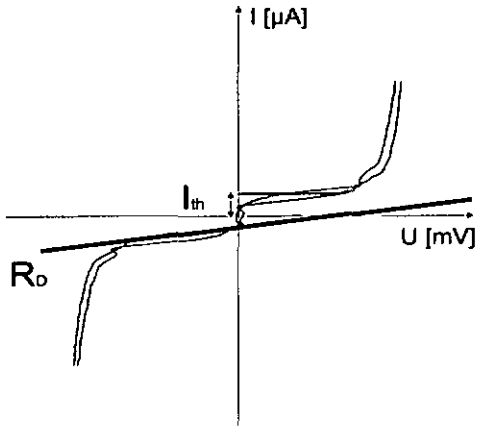

Fig. 5.3 : plot of the first I-V curve of figure 5.2 (not to scale).

With increased current scale and no applied magnetic field, one can measure the normal conducting resistance (R_N) and the Josephson current (I_J), as shown in figure 5.4 :

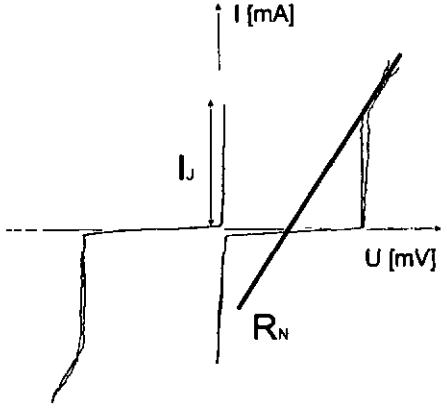

Fig. 5.4 : I-V curve whose scale was increased, showing the normal conducting resistance of the junction and the Josephson current (vertical).

From these curves, we calculated and obtained the following values :

Normal resistance	(R_N)	:	R_N	=	0.6	Ω
Dynamic resistance	(R_D)	:	R_D	=	1025	Ω
Thermal current	(I_{th})	:	I_{th}	=	750	nA
Josephson current	(I_J)	:	I_J	=	750	μA

Therefore we can calculate three important parameters, knowing that the surface A of one junction is 10^{-4} cm^2 :

Quality factor	(Q)	:	Q	=	$R_D / R_N = 1708$
Josephson current density	(I_J/A)	:	I_J/A	=	7.5 A·cm^{-2}
Conductance	$(R_N \cdot A)^{-1}$	:	$(R_N \cdot A)^{-1}$	=	$1.6 \cdot 10^4\ \Omega^{-1} \cdot$cm^{-2}

5.1.2. X-rays detected with our STJ

Before measuring macromolecules, we check the ability of our STJ to detect X-rays. We use a ^{55}Fe source, supplied by Nycomed Amersham, whose main lines are Mn-K_α = 5.89 keV and Mn-K_β = 6.49 keV. Its activity is 20 mCi (740 MBq) and it is deposited on a copper disc Ø 12.5 mm and 3 mm thick, covered with a nickel coating. It is mounted below the thermal shield located just above the STJ, directly irradiating them. Data[14] on the ^{55}Fe source are given in table 5.1.

A	Element	Z	Decay Mode	Half-life	Rad. Type	Radiation Energy (keV)	End-point Energy (keV)	Radiation Intensity %	Dose (G-RAD/UCI-H)
55	FE	26	EC	2.737 Y 0.011	E AU L	0.6100	139.	4	0.0018
55	FE	26	EC	2.737 Y 0.011	E AU K	5.190	60.7	0.7	0.0067
55	FE	26	EC	2.737 Y 0.011	G X L	0.6400	0.421	0.012	0
55	FE	26	EC	2.737 Y 0.011	G X Kα2	5.88765(3)	8.24	0.09	0.0010
55	FE	26	EC	2.737 Y 0.011	G X Kα1	5.89875(3)	16.28	0.18	0.0020
55	FE	26	EC	2.737 Y 0.011	G X Kβ	6.490	3.29	0.08	0.0005
55	FE	26	EC	2.737 Y 0.011	G	126.00 0.10	0		0

Table 5.1 : decay modes of the ^{55}Fe isotope.

[14] To retrieve data on radiation parameters, see : « http://www.nndc.bnl.gov/nndc/nudat/radform.html ».

When our junctions are in the proper operating conditions, we collect 6 keV X-ray events which we can display in a pulse height to rise time scatter plot, as shown in figure 5.5.

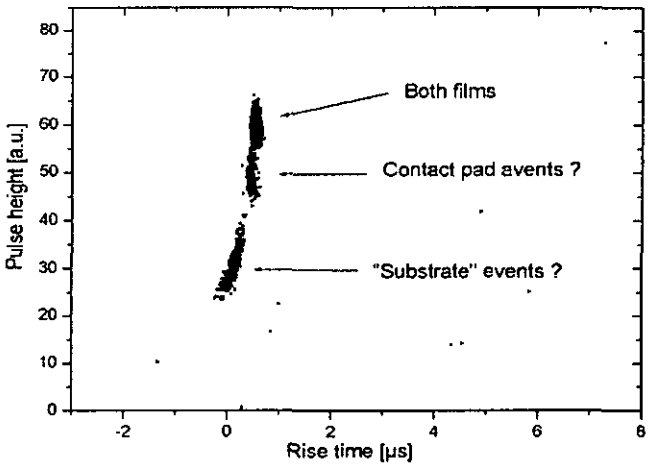

Fig. 5.5 : X-ray spectrum obtained with our STJ on a polyimide substrate. One should note that both films of the STJ and the substrate can interact with photons. To study carefully the X-rays, our type of substrate would not be very appropriate because its structure allows the propogation of phonons produced indirectly by the interaction with the X-ray photon.

From the above-spectrum, we obtain the following pulse height histogram :

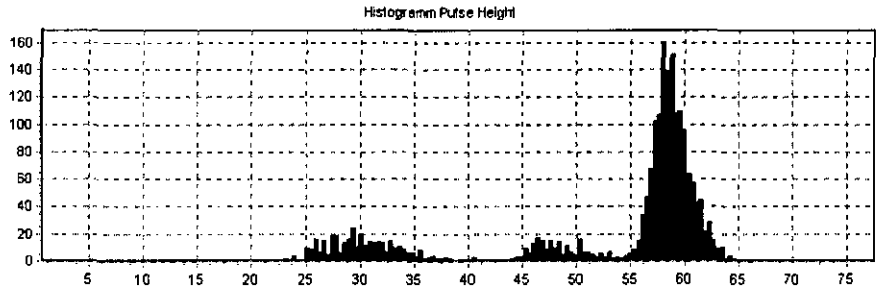

Fig. 5.6 : pulse height histogram of 6 keV events. Our relatively poor resolution does not allow us to resolve K_α and K_β.

5.1.3. Measurements of macromolecules

Before focusing on the comparison between different substrates, we measured several different types of macromolecule in order to calibrate and to run our new array.

We used light molecules (insulin) as well as heavier ones, like BSA or IgG.

The first spectrum, shown in figure 5.7, is a measurement of a Lyzozyme sample ($M_{Lys.}$= 14'300 Da) desorbed in liquid phase (liquid MALDI) by our IR laser. 1 mg of Lyzozyme was dissolved in 1 ml of 0.1% TFA solution. To prepare the matrix, 1 ml of sinapinic acid was dissolved in 0.6 ml of ethanol and 0.4 ml of deionized water. 0.5 ml of the Lyzozyme mixture was added to 1 ml of matrix and 100 µl of glycerol (final concentration : 21 pmol/µl), poured on the stainless steel sample holder and quickly put under vacuum.

We applied 16 kV on the first electrode and 15 kV on the second and recorded about 1350 events.

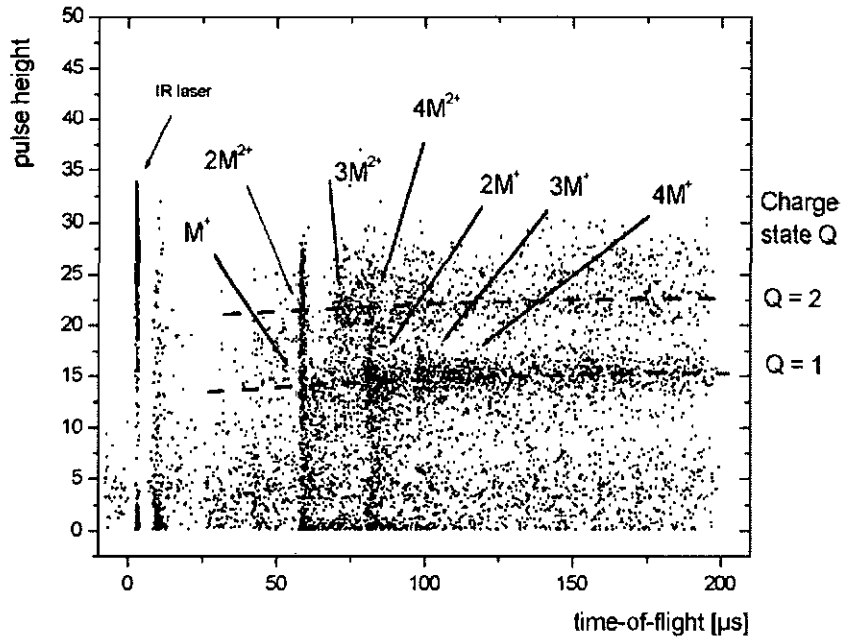

Fig. 5.7 : Lyzozyme spectrum obtained with our STJ on a polyimide substrate using an IR laser. The distance between the launch surface and the detectors was 80 cm.

The second example (figure 5.8) is a spectrum of Human Plasminogen Kringle 4 molecules (M = 9.695 kDa), obtained with a 337 nm UV laser (solid MALDI).

The mixture was prepared as follows : 1 mg of Hpgk4 was dissolved in 1 ml of deionized water : then 20 µl were mixed with 40 µl of matrix, previously prepared according to this recipe : 10 mg of sinapinic acid powder as matrix were dissolved in 0.6 ml of ethanol and 0.4 ml of deionized water. 5 µl of the « final » mixture (34 pmol/µl) were dried on the sample holder and put under vacuum.

The applied voltages were 16 kV and 11.1 kV (first and second electrode, respectively).

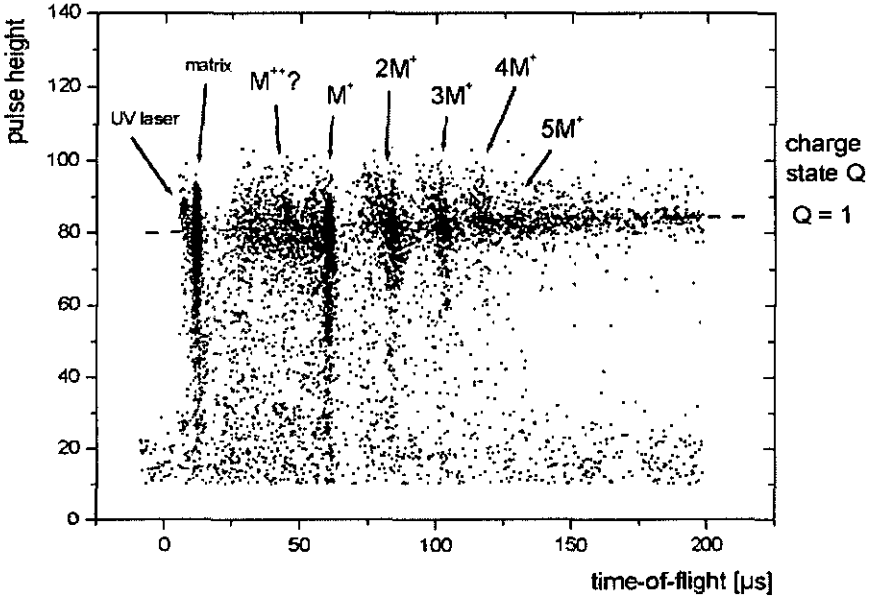

Fig. 5.8 : pulse height versus time-of-flight scatter plot for Hpgk4 molecules. Only the singly charged state was visible at this time, but the different masses are clearly separated. The fact that the doubly charged molecules produce the some pulse height as the singly charged molecules is an electronic artifact owing to the nonlinear response of the STJ-preamplifier system at the specific biasing condition.

5.1.4. Comparison between polyimide and glass substrates

We took spectra of the pulse height versus time-of-flight for different molecules. As mentioned above, the pulse height distribution has a nonlinear increase due to the large heating effect of the laser, which decreases the intensity of the signals close to the laser absorption time. This non-linear distribution is shown below by a dashed line. Note that we did not use molecules to analyze them but as a tool to measure the state of the detectors. Because the effect occurs at short times, we put high voltages on the electrodes, even if the cryodetectors are sensitive to low energetic ions.

Glass substrate

In order to be able to compare our different types of substrates, we performed earlier experiments with detectors fabricated on a glass substrate, 0.15 mm thick. We used glass, an amorphous structure, to reduce substrate events. The design was as follows : the glass substrate was pinched between the sample holder in copper and a PCB. Apiezon® grease insured a rather good thermal link (figure 5.9).

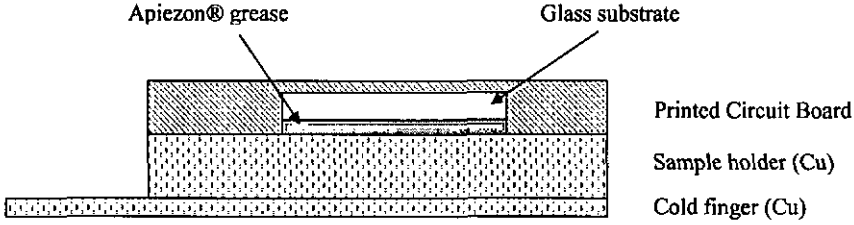

Fig. 5.9 : schematic of the assembly with glass substrate (not to scale).

This first sample on glass substrate was cooled in our dilution refrigerator (Kelvinox 25 from Oxford Instruments).

5.1.4.1. Results of the comparison with an IR laser (liquid MALDI)

Glass substrate

We used insulin molecules (M = 5'734.6 Da) with glycerol as the matrix (liquid MALDI). The mixture was introduced into the spectrometer through an array of 96 micromachined nozzles ($Ø_{nozzles}$= 4 μm) [14]. The laser was an IR laser supplied by LSI.

Figure 5.10 shows a pulse height versus time-of-flight scatter plot for STJ on a glass substrate. One can observe that for higher charged molecules, the decrease in pulse height for short time-of-flight values is more pronounced, leading to larger thermal recovery time. In this case, the detector has retrieved its full operational capability after 110 to 140 μs for Q = 2 [from 71].

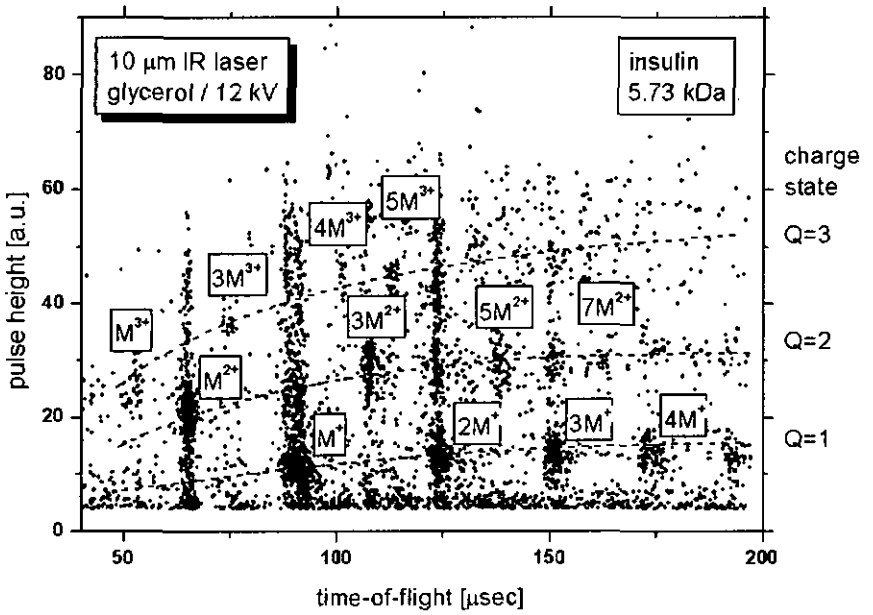

Fig. 5.10 : pulse height versus time-of-flight scatter plot for insulin. The pulse height distribution has a nonlinear increase due to the large heating effect of the IR laser.

Polyimide substrate on copper disc

We again used insulin molecules, launched from a liquid surface. We dissolved 1 mg of insulin powder in 1 ml of DMSO (dimethylsulfoxide). We took 400 µl of this solution and added 600 µl of glycerol (matrix). 5 µl (69 pmol/µl) were then dispensed on the sample holder and put under vacuum. Acceleration voltages of 12 and 11 kV were applied on the first and the second electrode, respectively.

We obtained the following spectrum (figure 5.11) :

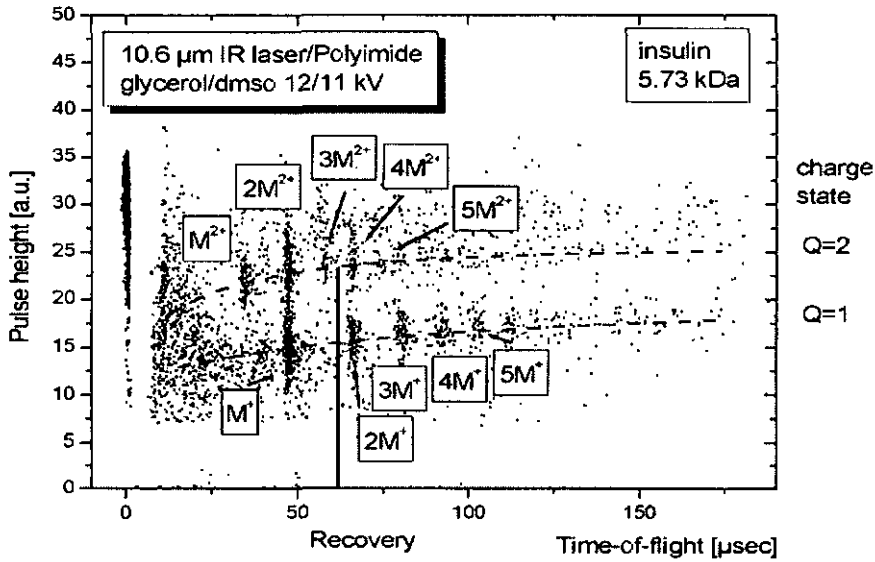

Fig. 5.11 : scatter plot obtained with insulin molecules detected by STJ on a polyimide substrate.

The peak at t = 0 is due to the reflexion of the IR pulse onto the detector (this reflection is used as a trigger). The matrix (glycerol (92 Da)) is detected after 7 µs.

The heating effect is more important due to the higher laser power which was not attenuated. A detailed look at the spectrum shows one main improvement compared to STJ on glass substrate (figure 5.10) : the junction retrieves its full capacity more rapidly than before. For Q = 2, STJ on a glass substrate recovered in about 110 µs (figure 5.10), whereas the recovery lasted only 60 µs for STJ on a polyimide substrate (see figure 5.11).

5.1.4.2. Results of the comparison with a UV laser (solid MALDI)

Glass substrate

We used Human Plasminogen Kringle 4 molecules (M = 9.695 kDa). 20 µl of Hpgk4 were mixed with 40 µl of matrix, previously prepared according to this recipe : 10 mg of sinapinic acid powder as matrix were dissolved in 0.6 ml of ethanol and 0.4 ml of deionized water. 5 µl of this mixture (34 pmol/µl) were dried on the stainless steel sample holder and put under vacuum. The two electrodes were at 16 and 8.6 kV. A UV laser was used to desorb the solution.

The recorded spectrum is shown in figure 5.12.

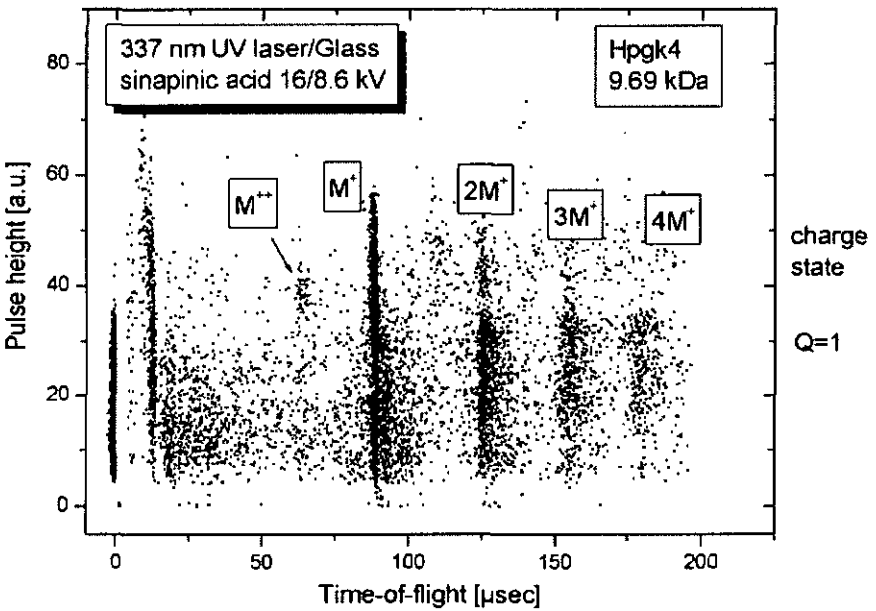

Fig. 5.12 : pulse height versus time-of-flight scatter plot of Hpgk4 molecules detected by STJ on a glass substrate.

Polyimide substrate on copper disc

The same mixture was prepared and dried on the sample holder. In this case, the electrodes were at 16 and 11.1 kV. 1500 events were recorded and plotted, as shown in figure 5.13.

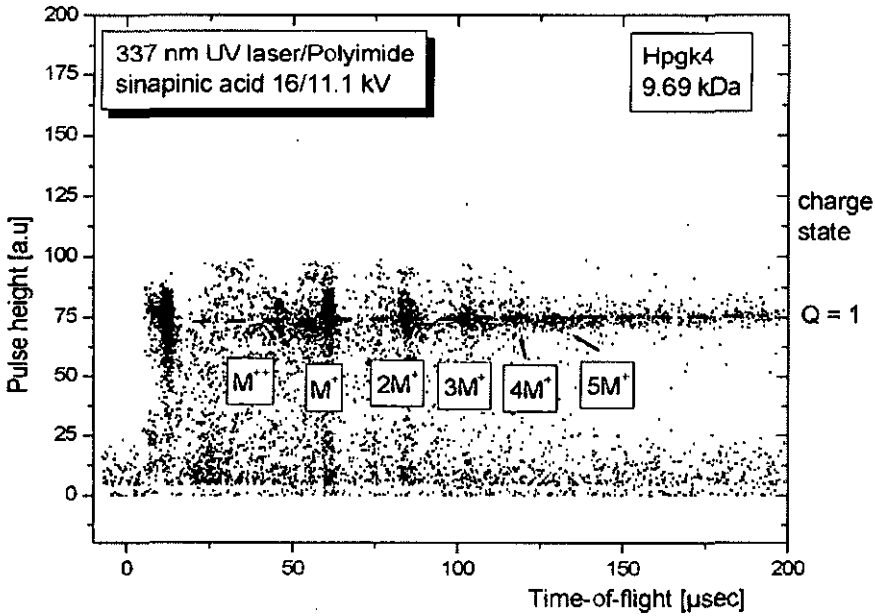

Fig. 5.13 : pulse height versus time-of-flight scatter plot af Hpgk4 molecules detected by STJ on o polyimide substrate.

The first peak is due to the matrix (molecular mass of sinapinic acid : M = 224 Da), which is detected after 14 µs. One observes that the pulse height distribution is almost constant and that the junctions already exhibit their full detection capability at short times (< 50 µs) : this is not the case for STJ on a glass substrate (figure 5.12) where the junctions have not recovered even after 150 µs.

Even if the UV laser is less powerful than the IR (see further), the local heating effect on the STJ is visible in figure 5.12, but not in the spectrum shown in figure 5.13. By using our new kind of substrate, the heating effect is reduced : the junctions have completely recovered when the first molecules arrive.

5.1.5. Conclusions

Both lasers (337 nm UV and 10.6 μm IR) locally heat the STJ, but the effect is much more pronounced for the IR laser, which is 60 times more powerful per laser shot. We can confirm that the recovery time of the STJ deposited on the polyimide layer is shorter and hence the pulse height of light or multicharged incoming molecules is less degraded. This is particularly important when the acceleration voltage is high, or when the flight distance is short.

The following observations deserve to be mentioned :

- *the dispersion of the pulse height, especially for* M^+ : the absorption of the laser light by the mixture is not constant for each pulse, leading to different intensities of reflected light onto the STJ, thus inducing signals whose pulse heights can vary.

- *the shape of the STJ pulses* : the signal is given by the collected charge Q which depends essentially on the tunneling time τ_{tun} and on the recombination time τ_{rec} which relies particularly upon the gap Δ , the critical temperature T_c and the temperature T. Plotting those expressions leads to a curve which is clearly related to the behavior of our STJ.

- *difference of behavior between the charge states* : some of the fastest molecules probably fragment and hence do not deposit their total initial energy. The heavier they are, the most probable and strong the process is, leading maybe to pulse shapes which are dependent on the mass of the molecules.

- *non-linear STJ-electronic response* : for certain STJ detectors and particular biasing conditions, the signals may become so large that in the case of current biasing, the signal response becomes nonlinear. In some cases the pulse heights of double charged molecules are as large as single charged molecules. A solution to this is to use an active voltage biased preamplifier scheme.

Future investigations will explain these effects in more detail.

We demonstrated that good junctions can be fabricated on a polyimide substrate. With this novel substrate, the STJ cool faster after the absorption of the intense laser pulse. Improvements can be further made by directly depositing the array onto the cold finger and so reducing the number of interfaces.

5.2. Energy transfer between X-ray and STJ / macromolecule and STJ

5.2.1. Calibrations

In this section we address the question how much of the absorbed molecule energy is converted into the STJ signal as compared to a 6 keV X-ray. The experiment was performed with Al STJ in the ADR and Ta STJ in the ^{3}He/^{4}He cryostat. In all experiments, a 6 keV X-ray source was continuously emitting X-rays. Whether our data acquisition collected events from X-rays or molecules depended on the specific trigger applied to the data acquisition card. When triggered on the UV laser event, virtually all signals were due to molecules. When turning off the laser and triggering on the pulses themselves, the events were always due to 6 keV X-rays.

We first made measurements with insulin with an acceleration voltage of exactly 6 kV, in order to transfer 6 keV to the molecules. The start signal was given by the external trigger of the laser. After a sufficient number of events, we only changed the trigger source to the acquisition channel in order to capture X-ray pulses, the setup remaining exactly the same. Results with Al STJ are given in section 5.2.1.1., whereas those for Ta STJ stand in section 5.2.1.2. Calibrations obtained in the past by other groups are discussed in section 5.2.1.3.

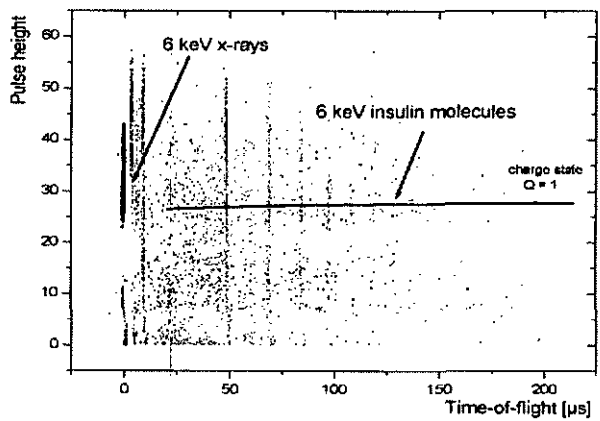

Fig. 5.14 : example of calibration of Al STJ on a polyimide substrate. The X-ray events are at time equal to zero. About 80 % of the kinetic energy of the molecule seem to be transferred to the detector.

5.2.1.1. Calibration of the Al STJ

The energy calibration of our Al STJ has been made in the manner as previously described. The results are shown in figure 5.15.

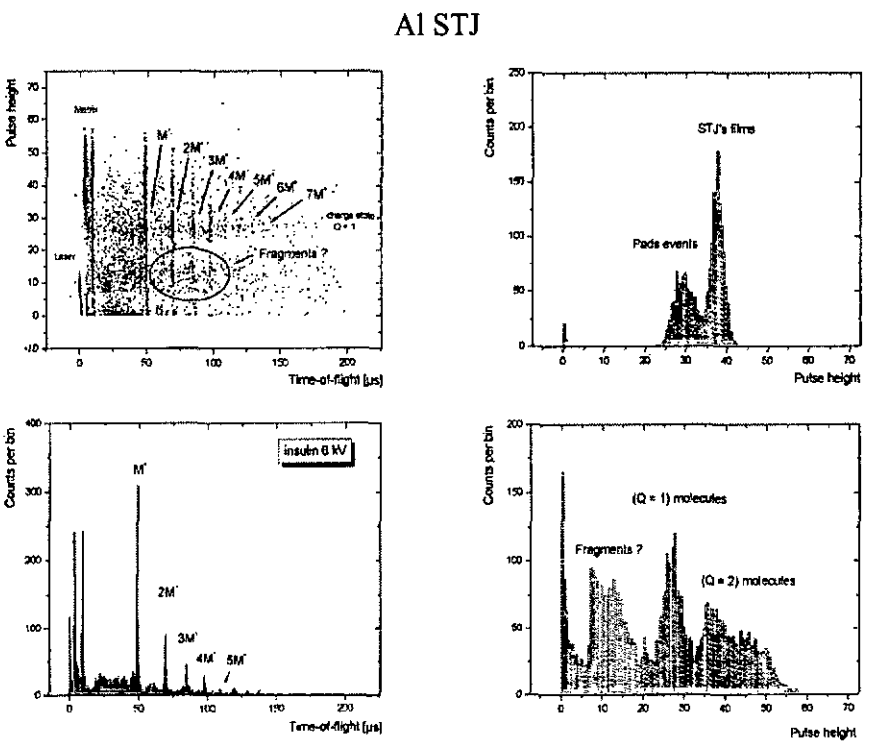

Fig. 5. 15 : left column : scotter plot (pulse height versus time-of-flight) and time-of-flight histogram of insulin molecules at 6 keV ; right column : comparison of the energy deposited in the detector by 6 keV X-rays and 6 keV insulin molecules.

We observe that we have a rather large dispersion in energy. However, the response of the detector to a 6 keV molecule seems to be 80% of the one for 6 keV X-rays.

5.2.1.2. Calibration of Ta STJ

For energy deposition calibration of a Ta STJ, we used our $^3He/^4He$ cryostat, as well as our new time-of-flight mass spectrometer. The Ta STJ, fabricated at PSI, have the following design :

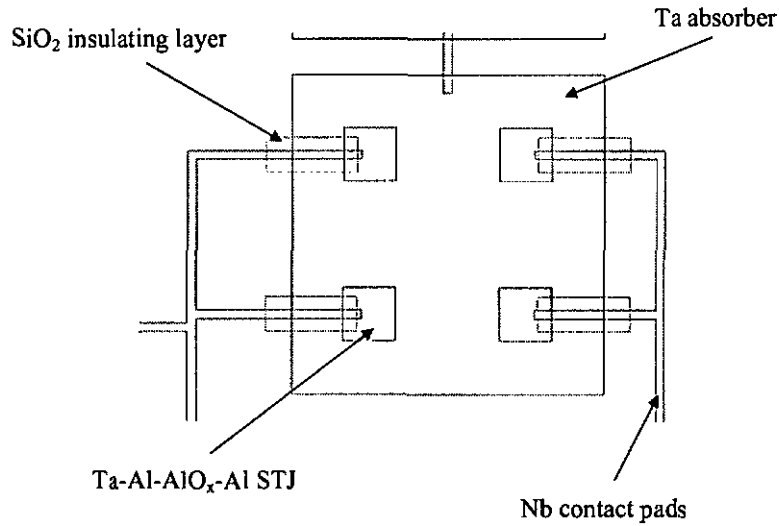

Fig. 5.16 : schematic of the PSI Ta STJ : the Ta absorber acts also as bottom film, a silicon dioxide layer isolates the contact pad from the absorber film.

Due to the fact that the surface of the absorber is large compared to the STJ, the probability for a X-ray photon to interact directly with the absorber is much greater. Thus there will be more events coming from the absorber than directly from the junction. However the absorber pulse heights will be smaller, because of the losses in it. This is shown in figure 5.17. An article on quasiparticle diffusion in tantalum can be found in [78].

In figure 5.18 one can note that the energy deposited in a Ta junction by a 6 keV X-ray and a 6 keV macromolecule is about the same.

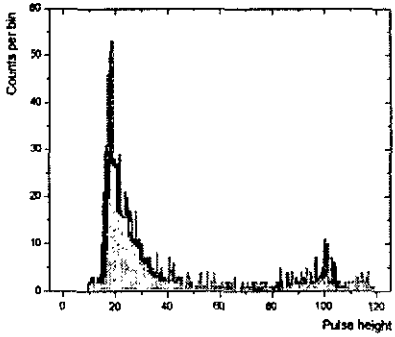

Fig. 5.17 : pulse height histogram of the X-ray spectrum obtained with Ta STJ. Most events come from interaction with the absorber (low energy), whereas the less frequent events from direct interaction with the junction are more energetic.

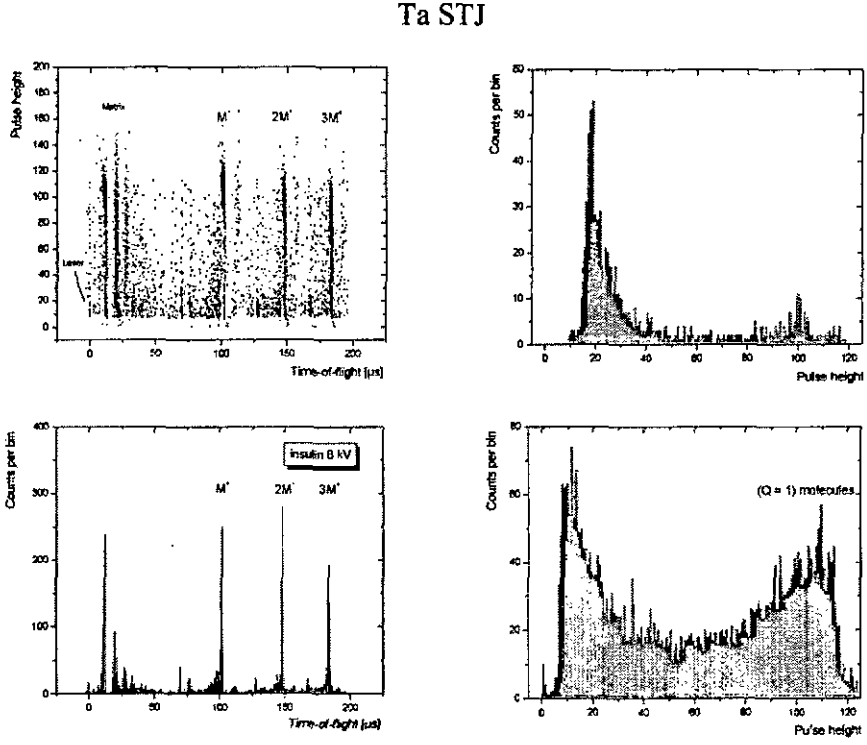

Fig. 5. 18 : left column : scatter plot (pulse height versus time-of-flight) and time-of-flight histogram of insulin molecules at 6 keV ; right column : comparison of the energy deposited in the detector by 6 keV X-rays and 6 keV insulin malecules.

5.2.1.3. Calibration of Sn, Nb and Al-AlO_x-Ag STJ

Similar X-ray/molecule comparisons have been made by us and other groups with other types of junctions : Sn STJ [IPH], Al-AlO_x-Ag NIS junctions [NIST] and Nb STJ [LLNL]. Results are presented below.

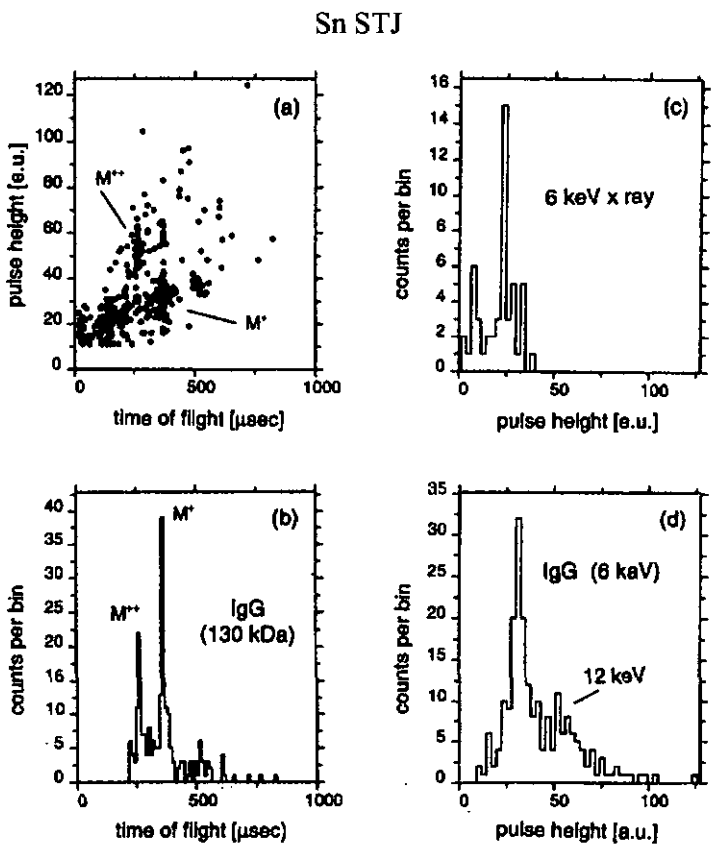

Fig. 5.19 : time-of-flight and pulse height histograms of IgG (135 kDa) at 6 kV acceleration voltoge. Comparisan of 6 keV pulse heights of ion impacts and X-ray hits (from [11]).

Wc can also see that the signal given by the Sn STJ is the same for 6 keV molecules and 6 keV X-rays.

In our experiment, described in the 1998 Nature paper [7], ions were detected with a microcalorimeter, consisting of a 100 nm thick silver absorber. The temperature rise owing to the molecule impact was detected as a current pulse produced by a NIS junction, which consisted of a thinly oxidized Al electrode in contact with the absorber. The ions (BSA in this case, m = 66.4 kDa) were accelerated to 20 kV. The pulse height versus time-of-flight spectrum is shown below in figure 5.20.

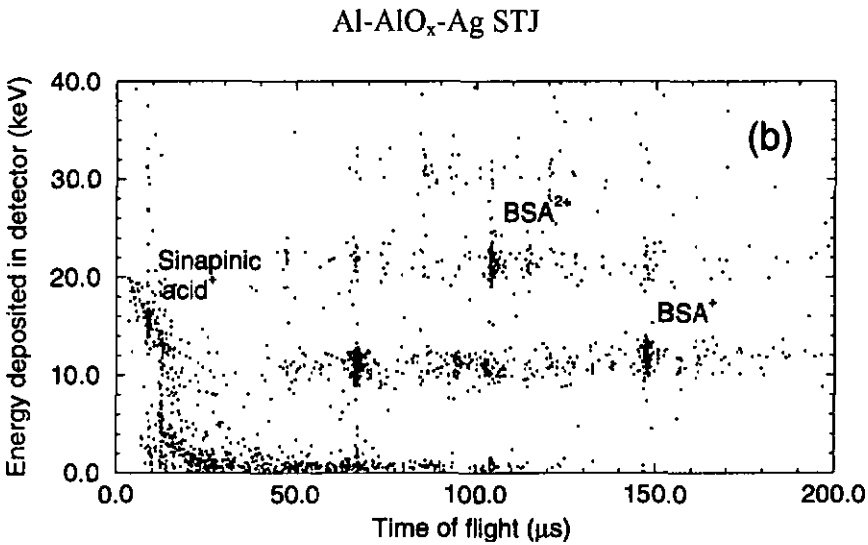

Fig. 5.20 : scatter plot of the energy deposited in the Ag microcalorimeter versus time-of-flight for 20 keV BSA molecules. One can note that half of the molecule energy is transferred into the detector.

The doubly charged molecules have, as expected, twice the energy of the singly charged ones. But only 50% of the kinetic energy is collected as inferred from calibrations with 6 keV X-rays.

This problem of different responses has already been discussed by Frank *et al.* [79]. They compared three kinds of cryogenic detectors regarding the pulse height signal for X-rays and molecules, as shown in the table below :

	Nb STJ	Sn STJ	Hot-electron Microcalorimeter
Operating temperature	~ 1.3 K	~ 0.5 K	~ 0.1 K
Phonon threshold	yes	yes, lower than Nb	no
Signal height relative to X-rays	~ 0.2	~ 1	~ 0.6
Energy resolution for X-rays	300 eV at 6 keV	180 eV at 6 keV	92 eV at 6 keV
Extrapolated resolution for biomolecules	~ 1.5 keV for 30 keV ions	180 eV for 6 keV ions	~ 215 eV for 20 keV ions
Measured energy resolution for biomolecules	~ 1.5 keV for 30 keV ions	~ 1.5 keV for 6 keV ions	1.7 keV for 20 keV ions
Obtained charge resolution $q/\Delta q$	~ 2	~ 4	~ 10

Table 5.2 : comparison of different types of cryogenic detectors used in mass spectrometry of macromolecules. Sn STJ results are from Gerber [11], Nb STJ results from Frank et al. [79] and « hot-electron micracalorimeter » results from Hilton et al. [7] (table from [79]).

We can now add our Al STJ results (~ 0.8) and Ta STJ results (~ 1) to this list :

STJ	Sn	Nb	Al	Ta	Hot-electron microcalorimeter
Relative signal between X-rays and macromolecules	~ 1	~ 0.2	~ 0.8	~ 1	~ 0.6

Table 5.3 : results of calibrations between signals given by X-rays and molecules for different materials.

The ratio is thus very different from one to another material, ranging from 20% to almost 100%. Possible explanations are given in the following section.

5.2.2. Energy transfer in a STJ detector

The energy absorbed by an X-ray or a macromolecule hitting a STJ detector leads to different processes in the films of the STJ. An X-ray can penetrate and interact in both films, or even in the substrate whereas the macromolecules interact only on the surface of the top superconducting film. A good description of the interaction of an X-ray photon by the photoelectric effect is given in [52, 70]. One knows that for an X-ray about 60% of the energy is converted into excess quasiparticles, whereas the remaining energy is converted into phonons, according to distributions well described in [80].

The case is different for macromolecules : when hitting the surface, macromolecules create high-energy phonons. One can distinguish two categories of phonons : those with an energy lower than twice the gap ($\hbar\omega < 2 \cdot \Delta$) and those with a energy higher ($\hbar\omega \geq 2 \cdot \Delta$). The former will not be able to break Cooper pairs and thus do not create excess quasiparticles which produce the detector signal owing to the tunnel effect.

One can question whether the relative signal between X-rays and molecules is dependent on the gap : values for the materials we are interested in are written in table 5.4. Superconducting materials with a gap smaller than 1 meV seem to have a signal ratio of 1. But this hypothesis was not confirmed by the hot-electron microcalorimeter experiment for which there is no gap at all.

Hilton *et al.* [7] discussed the possibility of breaking of molecular bonds upon impact and ejection of molecular fragments as effects to explain the reduced energy deposited into the microcalorimeter. But, there is no immediate reason to think this could not happen to other kinds of junctions.

A possible explanation is the difference in the phonon spectra of the various metals and in the complicated energy and time dependent interactions between the phonons and electrons, notably for the strong non-equilibrium conditions directly following the energetic particle absorption event. This is an interesting topic for future investigations.

STJ	Sn	Nb	Al	Ta	Hot-electron microcalorimeter[15]
Critical temperature [K]	3.7	9.2	1.2	4.5	1.2
Energy gap (Δ) [meV] at T = 0 K	0.59	1.47	0.17	0.69	non existing
Relative signal between X-rays and macromolecules	~ 1	~ 0.2	~ 0.8	~ 1	~ 0.6

Table 5.4 : data far different materials and results af calibration.

[15] The critical temperature for the superconducting material of the NIS junction, aluminum in this case.

Conclusions

In this work we developed a new kind of Al STJ array, deposited on different types of substrates, either glass or polyimide. The advantage of these arrays is that they are easy to fabricate. They were tested in our little ^{3}He/^{4}He cryostat and cooled down in our dilution refrigerator, ^{3}He/^{4}He or ADR.

We showed that 6 keV X-rays can be detected with the STJ on both polyimide and glass substrates, as well as several kinds of macromolecules (insulin, Lyzozyme, BSA, IgG, Hpgk4, etc). We demonstrated the ability of STJ on the polyimide substrate to recover more rapidly from the heat deposited by the laser pulse due to better thermalization.

We proposed the following improvements for future work :

- concerning the Al STJ : the photolithographic process can be improved, in order to increase the reproducibility of the junctions. A better choice of photoresist and a search for the optimum developing and etching baths could lead to a more precise structuring. The use of high-purity oxygen to create the oxide barrier as well as the optimization of the thickness of the Al layers have to be considered in the future.

- concerning polyimide substrates : in order to prevent the thermal and mechanical « problems » when pinching the copper disc, a new kind of « substrate » is currently under construction. Combining the sample holder and the copper disc at the same time, it is shown in figure c.1.

Gallium arsenide substrates have been fabricated with a MBE and prepared for the deposition. The aim of this substrate is to make a « phonon filter » which prevents the low-energy phonons to reach the STJ and retains those with a high energy. A better stability of the junctions is expected. In the future, STJ on such substrates will be tested and the stack of layers optimized for a maximum filtering capability.

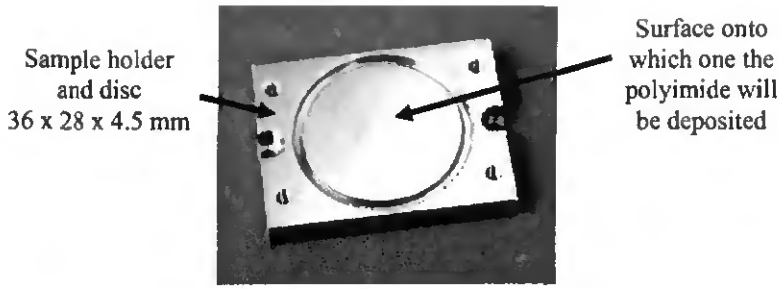

Fig. c.1 : new kind of capper sample holder which can be self-mounted onto the cold finger, reducing the number of interfaces. The polyimide will be deposited on the central part and the STJ fabricated in the same way as before. A PCB will be screwed onto it in order to connect the junctions.

Concerning the calibrations of the molecule signals with 6 keV X-rays, a more detailed study of the results obtained with Ta junctions should be made. It would be interesting to investigate the difference between Al-AlO_x-Ag and Nb STJ and the other STJ to find out the reason(s) for the differences in deposited energy. This could be achieved by carefully trying to understand the exact mechanism of energy deposition from a macromolecule into a STJ.

References

[1] M. Karas, D. Bachmann, U. Bahr and F. Hillenkamp, *Matrix-assisted ultraviolet laser desorption of non-volatile compounds*, Int. J. Mass Spectrom. Ion Proc. **78** (1987) 53-68

[2] D. Twerenbold, *Biopolymer mass spectrometer with cryogenic particle detectors*, Nucl. Inst.&Meth. A **370** (1996) 253-255

[3] G. Gervasio, D. Gerber, D. Gritti, Y. Gonin, D. Twerenbold, J.-L. Vuilleumier, *Aluminum junctions as macromolecule detectors and comparison with ionizing detectors*, Nucl. Inst.&Meth. A **444** (2000) 389-394

[4] D. Twerenbold, D. Gerber, D. Gritti, Y. Gonin, A. Netuschill, F. Rossel, D. Schenker, J.-L. Vuilleumier, *Single molecule detector for mass spectrometry with mass independent detection efficiency*, Proteomics 2001, **1**, 66-69

[5] D. Gritti, *Mass Spectrometry with Cryogenic Detectors*, PhD Thesis, University of Neuchâtel, 2001

[6] D. Twerenbold, J.-L. Vuilleumier, D. Gerber, A. Tadsen, B. van den Brandt, P.M. Gillevet, *Detection of single macromolecules using a cryogenic particle detector coupled to a biopolymer mass spectrometer*, Appl. Phys. Lett. **68** (24) (1996) 3503-3505

[7] G.C. Hilton, John M. Martinis, D.A. Wollman, K.D. Irwin, L.L. Dulcie, D. Gerber, P.M. Gillevet, D. Twerenbold, *Impact energy measurement in time-of-flight mass spectrometry with cryogenic microcalorimeters*, Nature **391** (1998) 672-675

[8] G.C. Hilton, J.M. Martinis, D. Twerenbold, P.M. Gillevet, D.A. Wollman, K.D. Irwin, L.L. Dulcie, D. Gerber, *Microcalorimeter particle detector for mass spectrometry*, talk given by G.C. Hilton at LTD-7 Conference, Munich, 1997

[9] D. Gerber, C. Grosjean, D. Twerenbold, J.-L. Vuilleumier, P.M. Gillevet, B. van den Brandt, *Cryogenic particle detectors in biopolymer mass spectrometers*, p. 73-75 in [35]

[10] M. Frank, C.A. Mears, S.E. Labov, W.H. Benner, D. Horn, J.M. Jaklevic, A.T. Barfknecht, *High-efficiency detection of 66 000 Da protein molecules using a cryogenic detector in a matrix-assisted laser desorption/ionization time-of-flight mass spectrometer*, Rapid. Commun. Mass Spectrom. **10** (1996) 1946-1950

[11] D. Gerber, *Cryogenic Detectors as High-Efficiency Detectors of Single Massive Macromolecules*, PhD Thesis, University of Neuchâtel, 1997

[12] M.W. Senko, F.W. Lafferty, *Mass spectrometry of macromolecules : has its time now come ?*, Annu. Rev. Biophys. Biomol. Struct. **23** (1994) 763-785

[13] R.J. Cotter, *Time-of-Flight Mass Spectrometry*, American Chemical Society, 1997

[14] Ph. Luginbuhl, P.-F. Indermuhle, M.-A. Grétillat, F. Willemin, N.F. de Rooij, D. Gerber, G. Gervasio, J.-L. Vuilleumier, D. Twerenbold, M. Düggelin, D. Mathys, R. Guggenheim, *Femtoliter injector for DNA mass spectrometry*, Sensors and Actuators B **63** (2000) 167-177

[15] H. Kamerlingh Onnes, Comm. Phys. Lab., University of Leiden, **119b**, **120b**, **122b**, **124c** (1911)

[16] W. Meissner, R. Ochsenfeld, *Ein neuer Effekt bei Eintritt der Supraleitfähigkeit*, Naturwissenschaften **21** (1933) 787-788

[17] F. and H. London, *The Electromagnetic Equations of the Supraconductor*, Proc. Roy. Soc. (London) A **149** (1935) 71-88

[18] F. und H. London, *Supraleitung und Diamagnetismus*, Physica **2** (1935) 341-354

[19] H. Fröhlich, *Theory of the Superconducting State. I. The Ground State at the Absolute Zero of Temperature*, Phys. Rev. **79** (5) (1950) 845-856

[20] E. Maxwell, *Isotope Effect in the Superconductivity of Mercury*, Phys. Rev. **78** (1950) 477

[21] C.A. Reynolds, B. Serin, W.H. Wright, L.B. Nesbitt, *Superconductivity of Isotopes of Mercury*, Phys. Rev. **78** (1950) 487

[22] A.B. Pippard, *An experimental and theoretical study of the relation between magnetic field and current in a superconductor*, Proc. Roy. Soc. (London) A **216** (1953) 547-568

[23] L.N. Cooper, *Bound Electron Pairs in a Degenerate Fermi Gas*, Phys. Rev. **104** (4) (1956) 1189-1190

[24] J. Bardeen, L.N. Cooper, J.R. Schrieffer, *Theory of Superconductivity*, Phys. Rev. **108** (5) (1957) 1175-1204

[25] M. Tinkham, *Introduction to superconductivity*, McGraw-Hill, New-York, 1975

[26] D.G. McDonald, *The Nobel Laureate versus the Graduate Student*, Physics Today (July 2001) 46-51

[27] D. Twerenbold, *Cryogenic particle detectors*, Rep. Prog. Phys. **59** (1996) 349-426

[28] N.E. Booth, B. Cabrera. E. Fiorini, *Low-temperature particle detectors*, Annu. Rev. Nucl. Part. Sci. **46** (1996) 471-532

[29] *Proceedings of the Workshop on Low Temperature Detectors for Neutrinos and Dark Matter*, eds. K. Pretzl, N. Schmitz, L. Stodolsky, Springer-Verlag, Berlin Heidelberg, 1987

[30] *Proceedings of the Second European Workshop on Low Temperature Devices for the Detection of Low Energy Neutrinos and Dark Matter*, eds. L. Gonzalez-Mestres, D. Perret-Gallix, Frontières, Gif-sur-Yvette, France, 1988

[31] *Proceedings of the Third International Workshop on Low Temperature Detectors for Neutrinos and Dark Matter*, eds. L. Briogato, D.V. Camin, E. Fiorini, Frontières, Gif-sur-Yvette, France, 1990

[32] *Proceedings of the Fourth International Workshop on Low Temperature Detectors for Neutrinos and Dark Matter*, eds. N.E. Booth, G.L. Salmon, Frontières, Gif-sur-Yvette, France, 1992

[33] *Proceedings of the Fifth International Workshop on Low Temperature Detectors*, eds. B.A. Young, S.E. Labov, J. of Low Temp. Phys. **93** (1993) 185-858

[34] *Proceedings of the Sixth International Workshop on Low Temperature Detectors (LTD-6)*, eds. H.R. Ott, A. Zehnder, Nucl. Inst.&Meth. A **370** (1996)

[35] *Proceedings of the Seventh International Workshop on Low Temperature Detectors (LTD-7)*, ed. S. Cooper, Munich, 1997

[36] *Proceedings of the Eighth International Workshop on Low Temperature Detectors (LTD-8)*, eds. P. de Korte, T. Peacock, Nucl. Inst.&Meth. A 444 (2000)

[37] *Proceedings of the Ninth International Workshop on Low Temperature Detectors (LTD-9)*, eds. F.S. Porter, D. McCammon, M. Galeazzi, C.K. Stahle, AIP Conference Proceedings **605** (2002)

[38] E. Fiorini, T.O. Niinikoski, *Low-temperature calorimetry for rare decays*, Nucl. Inst.&Meth. **224** (1984) 83-88

[39] S.H. Moseley, J.C. Mather, D. McCammon, *Thermal detectors as X-ray spectrometers*, J. Appl. Phys. **56** (5) (1984) 1257-1262

[40] E.E. Haller, *Isotopically engineered semiconductors*, J. Appl. Phys. 77 (7) (1995) 2857-2878

[41] C. Brofferio, *The CUORE/CUORICINO Project, Preliminary Studies*, Physics of Atomic Nuclei 63 (7) (2000) 1259-1263

[42] B.A. Young, B. Cabrera, A.T. Lee, B.L. Dougherty, *Detection of elementary particles using silicon crystal acoustic detectors with titanium transition edge phonon sensors*, Nucl. Inst.&Meth. A **311** (1992) 195-216

[43] M. Nahum, J.M. Martinis, *Hot-electron microcalorimeters as high-resolution X-ray detectors*, Appl. Phys. Lett. **66** (23) (1995) 3203-3205

[44] M. Nahum, T. M. Eiles, J.M. Martinis, *Electronic microrefrigerator based on a normal-insulator-superconductor tunnel junction*, Appl. Phys. Lett. **65** (24) (1994) 3123-3125

[45] K.D. Irwin, *An application of electrothermal feedback for high resolution cryogenic particle detection*, Appl. Phys. Lett. **66** (15) (1995) 1998-2000

[46] H. Bernas, J.P. Burger, G. Deutscher, C. Valette, S.J. Williamson, *Destruction of superconducting metastable states by β^- irradiation*, Phys. Lett. **24A** (13) (1967) 721-722

[47] L. Gonzalez-Mestres, D. Perret-Gallix, *Basic properties of superheated superconducting granules detectors*, pp. 297-320, in [30]

[48] M. Abplanalp, C. Berger, G. Czapek, U. Diggelmann, M. Furlan, A. Gabutti, S. Janos, U. Moser, R. Pozzi, K. Pretzl, K. Schmiemann, D. Perret-Gallix, B. van den Brandt, J.A. Konter, S. Mango, *Detection of nuclear recoils in prototype dark matter detectors, made from Al, Sn and Zn superheated superconducting granules*, Nucl. Inst.&Meth. A **360** (1995) 616-625

[49] I. Giaver, *Energy gap in superconductors measured by electron tunnelling*, Phys. Rev. Lett. **5** (4) (1960) 147-148

[50] I. Giaver, *Electron tunneling between two superconductors*, Phys. Rev. Lett. **5** (10) (1960) 464-466

[51] G.H. Wood, B.L. White, *Pulses induced in tunneling currents between superconductors by alpha-particle bombardment*, Appl. Phys. Lett. **15** (8) (1969) 237-239

[52] D. Twerenbold, A. Zehnder, *Superconducting Sn/Sn-oxide/Sn tunneling junctions as high-resolution X-ray detectors*, J. Appl. Phys. **61** (1) (1987) 1-7

[53] D. Twerenbold, *Giaver-Type Superconducting Tunnelling Junctions as High-Resolution X-ray Detectors*, PhD Thesis, ETH Zurich, 1986

[54] D. Twerenbold, *Giaver-Type Superconducting Tunnelling Junctions as High-Resolution X-ray Detectors*, Europhys. Lett **1** (5) (1986) 209-214

[55] M. Van den Berg, *Development of a High Resolution X-ray Spectrometer based on Superconductive Tunnel Junctions*, PhD Thesis, SRON, Netherlands, 1999

[56] K. Segall, C. Wilson, L. Frunzio, L. Li, S. Friedrich, M.C. Gaidis, D.E. Prober, A.E. Szymkowiak, S.H. Moseley, *Noise mechanisms in superconducting tunnel-junction detectors*, Appl. Phys. Lett. **76** (26) (2000) 3998-4000

[57] T. Imamura, T. Shiota, S. Hasuo, *Fabricotion of High Quality Nb/AlO_x-Al/Nb Josephson Junctions : I-Sputtered Nb Films for Junction Electrodes*, IEEE Trans. Appl. Supercond. 2 (1) (1992) 1-14

[58] W. Ootani, T. Ikeda, H. Kato, K. Kawai, H. Miyasaka, T. Oku, C. Otani, H. Sato, H.M. Shimizu, Y. Takizawa, H. Watanabe, H. Nakagawa, H. Akoh, M. Aoyagi, T. Taino, *Development of X-ray detectors based on Nb/Al/AlO_x/Nb superconducting tunnel junctions*, Nucl. Inst.&Meth. A **444** (2000) 249-252

[59] A. Poelaert, A. Peacock, N. Rando, P. Verhoeve, P. Videler, *The suppression of phonon induced noise in niobium superconducting tunnel junctions X-ray detectors*, J. Appl. Phys. 79 (5) (1996) 2574-2579

[60] H. Sato, T. Ikeda, H. Kato, K. Kawai, H. Miyasaka, T. Oku, W. Ootani, C. Otani, H.M. Shimizu, H. Watanabe, H. Nakagawa, H. Akoh, M. Aoyagi, T. Taino, K. Inaba, Y. Kino, *Development of Superconducting tunnel junctions with an Aluminum-Oxide Insulation Layer for X-ray Detection*, IEEE Trans. Appl. Supercond. 9 (2) (1999) 4475-4478

[61] H. Sato, Y. Takizawa, W. Ootani, T. Ikeda, T. Oku, C. Otani, H. Watanabe, K. Kawai, H. Miyasaka, H. Kato, H.M. Shimizu, H. Nakagawa, H. Akoh, M. Aoyagi, T. Taino, *Improved Fabrication Method for Nb/Al/Alo_x/Al/Nb Superconducting Tunnel Junctions as X-ray Detectors*, Jpn. J. Appl. Phys. 39 (2000) 5090-5094

[62] G. Angloher, M. Huber, J. Jochum, F. von Feilitzsch, R.L. Mössbauer, G. Safran, *Effects of quasiparticle recombination and photoelectron escape in Al- Superconducting tunnel junction detectors*, J. of Low Temp. Phys. **123** (3, 4) (2001) 165-180

[63] M. Kurakado, *Possibility of high resolution detectors using superconducting tunnel junctions*, Nucl. Inst.&Meth. **196** (1982) 275-277

[64] L. Solymar, *Superconductive Tunnelling and Applications*, Chapman and Hall Ltd, London, 1972

[65] D. Twerenbold, *Superconducting tunneling junctions as X-ray detectors and their possible applications in astrophysics*, Nucl. Inst.&Meth. A **273** (1988) 575-582

[66] K.E. Gray, *A superconducting transistor*, Appl. Phys. Lett. **32** (6) (1978) 392-395

[67] B.D. Josephson, *Possible new effects in superconductive tunneling*, Phys. Lett. **1** (7) (1962) 251-253

[68] A. Barone, G. Paterno, *Physics and Applications of the Josephson Effect*, Wiley-Interscience, New-York, 1982

[69] D.D. Coon, M.D. Fiske, *Josephson ac and Step Structure in the Supercurrent Tunneling Characteristic*, Phys. Rev. **138** (3A) (1965) A744-A746

[70] D. Twerenbold, *Nonequilibrium model of the superconducting tunneling junction X-ray detector*, Phys. Rev. B **34** (11) (1986) 7748-7759

[71] D. Twerenbold, A. Netuschill, N.F. de Rooij, Ph. Luginbuhl, D. Gerber, D. Gritti, Y. Gonin, F. Rossel, J.-L. Vuilleumier, *Detecting single molecules launched from liquid surfaces in a time-of-flight mass spectrometer using ultraviolet and infrared lasers*, Proteomics 2002, 2, 436-440

[72] Y. Gonin, D. Gerber, D. Gritti, A. Netuschill, D. Schenker, D. Twerenbold, J.-L. Vuilleumier, *Reducing thermal recovery time after a laser pulse of superconducting tunnel junctions acting as sensors for time-of-flight mass spectrometry*, not yet published

[73] V. Narayanamurti, H.L. Störmer, M.A. Chin, A.C. Gossard, W. Wiegmann, *Selective Transmission of High-Frequency Phonons by a Superlattice : The « Dielectric » Phonon Filter*, Phys. Rev. Lett. **43** (27) (1979) 2012-2016

[74] D.L. Meier, J.X. Przybysz, J. Kang, *Fabrication of an all-refractory circuit using lift-off with imoge-reversal photoresist*, IEEE Trans. Magn. **27** (2) (1991) 3121-3124

[75] Y. Gonin, *Fabrication d'un réseau de jonctions supraconductrices comme détecteurs de macromolécules et fabrication d'un évaporateur à canon à électrons U.H.V.*, Diploma thesis, University of Neuchâtel, 1998

[76] F. Pobell, *Matter and Methods at Low Temperatures*, Springer-Verlag, Berlin, 1996

[77] O.V. Lounasmaa, *Experimental Principles and Methods Below 1 K*, Academic Press, London and New-York, 1974

[78] T. Nussbaumer, Ph. Lerch, E. Kirk, A. Zehnder, R. Fücbslin, P.F. Meier, H.R. Ott, *Quasiparticle diffusion in tantalum using superconducting tunnel junctions*, Phys. Rev. B **61** (14) (2000) 9719-9728

[79] M. Frank, S.E. Labov, G. Westmacott, W.H. Benner, *Energy-sensitive cryogenic detectors for high-mass biomolecule mass spectrometry*, Mass Spectrometry Reviews **18** (1999) 155-186

[80] A. Zehnder, *Response of superconductive films to localized energy deposition*, Phys. Rev. B **52** (17) (1995) 12 858-12 866

Acknowledgments

I would like first to thank Prof. **J.-L. Vuilleumier** for his support throughout this thesis.

Damian, thanks for allowing me to join this great project, for all your enthusiasm and scientific competence.

Despite his rare bad mood, his occasional depressive state and legendary pessimism, he was the one who guided me througbout this task and permitted me to fulfill our mission : thank you, **Danou**, for all these enlightening discussions, your « always wise advices », hard work in the cleanroom and for your wide range of « music ».

Thanks to **Domi** for his scientific, technical and human competences, for his always good mood and humor and for his last moanings « Y'm'faut un job, b... », except concerning his « Poupinette » and « Chopine (or Schmoey) ».

Warm thanks are also addressed to **Alex**, our MALDI man, **Dom**, the decaffeinated sailor, and **Fred**, our stock-options and finance specialist, for their support, competence and friendship.

I would like also to thank **Jose** (Rosssssssssssséééééééééééééééé) for a lot of measurements undertaken together and for the so many times I disturbed him by entering violently in his office.

Thanks also to the other part of the Particle Physics group : **Roland**, **Vérène**, **Jean-Michel**, **Gogy** (Danou's dear wife), **Patrick**, **Zori**, **Leila**, **Frédéric**, **Ioszef**, **Giovanni**.

My gratitude goes also to **Ricardo**, the man with a hammock, for the great collaboration we had for a precise projeet and to my colleagues at IPH.

Thanks to the technical staff (**Christian**, **Francis**, **Idyne**, **André**, **Kouni**, **Toti**, **Urs Bart**, **René**, **Etienne**, **Daniel**, **Thierry Delhove** and **Jean-Louis**) for the incredible number of things they did for us, to the administration (**Patty**, **Sonia**, **Gina**, **Anne-Marie**, **Muriet** and **Gianfranco di Rocco**) for their support. I would not like to be ungrateful by forgetting those who are bursars of the building

(**Thierry R.**, **Eugenio** (Leone) and **Thierry M.**), always, but not often remarked, very useful. Thank you all !

Thank you also to the members of the jury, those above-mentioned and *Dr.* **Eugenie Kirk**, from PSI, for having taken time to be part of it.

Let me be also thankful to friends « around », especially my « Audi S4 friend » (**Jamil**).

I would like to thank my family for the great time we have together and their support during those long years.

Finally, last but for sure not least, I thank from all my heart my dear wife **Cynthia** and the most wonderful gift I ever received, my daughter **Chloé**.